THE ASTROPHYSICAL JOURNAL, 425:14–34, 1994 April 10

DISCOVERY OF CEPHEIDS IN IC 4182: ABSOLUTE PEAK BRIGHTNESS OF SN Ia 1937C AND THE VALUE OF H_0[1]

A. SAHA
Space Telescope Science Institute, 3700 San Martin Drive, Baltimore, MD 21218

LUKAS LABHARDT AND HANS SCHWENGELER
Astronomisches Institut der Universität Basel, Venusstrasse 7, CH-4102 Binningen, Switzerland

F. D. MACCHETTO[2] AND N. PANAGIA[2,3]
Space Telescope Science Institute, 3700 San Martin Drive, Baltimore, MD 21218

ALLAN SANDAGE
Observatories of the Carnegie Institution of Washington, 813 Santa Barbara Street, Pasadena, CA 91101

AND

G. A. TAMMANN
Astronomisches Institut der Universität Basel, Venusstrasse 7, CH-4102 Binningen, Switzerland; and European Southern Observatory, Garching bei München, Germany

Received 1993 June 29; accepted 1993 October 13

ABSTRACT

Repeated imaging of a field in the Sdm galaxy IC 4182 with the Wide Field Camera of the *Hubble Space Telescope* has led to the discovery of 28 Cepheid variables. The distance modulus to this galaxy, derived from the Cepheids, is $(m - M) = 28.36 \pm 0.09$, and the absolute magnitude at peak brightness of the Type Ia supernova SN 1937C which appeared in IC 4182 is $M_V(\max) = -19.72 \pm 0.13$. The Hubble diagram using peak V magnitudes of distant (Virgo cluster and beyond) Type Ia supernovae (selected a priori on the basis of light curve and spectral conformity with the prototype) shows an observational random scatter of 0.36 mag, with evidence that the intrinsic scatter is even smaller. Using the observed scatter to estimate the uncertainty of calibrating the Hubble diagram using only the single calibrating supernova SN 1937C, it is shown that $H_0 = 52 \pm 9$ km s^{-1} Mpc^{-1}.

Subject headings: Cepheids — cosmology: observations — distance scale — galaxies: individual (IC 4182) — stars: individual (SN 1937C)

1. INTRODUCTION

IC 4182 is a nearby Sdm galaxy (R.A.$_{1950} = 13^h03^m30^s$, decl.$_{1950} = +37°52'23''$) at high Galactic latitude ($l = 108°$, $b = +79°$). It is very nearly face-on, has recession velocity $v_0 = 344 \pm 4$ km s^{-1} and integrated brightness $B_T = 13.0$. It produced the prototypical Type Ia supernova (SN Ia) SN 1937C (Baade & Zwicky 1938).

Following the initial demonstration by Kowal (1968), most rediscussions have confirmed that such SNe Ia show small intrinsic dispersion in their luminosities at maximum light (Barbon, Capaccioli, & Ciatti 1975; Branch & Bettis 1978; Tammann 1982; Branch 1982; Cadonau, Sandage, & Tammann 1985; Tammann & Leibundgut 1990; Miller & Branch 1990; Della Valle & Panagia 1992) and are therefore good standard candles. Also, they are the brightest beacons that allow us to probe out to cosmological distances, where the effect of the peculiar motions due to inhomogeneities from galaxy clustering is insignificant compared to the larger velocities from the Hubble flow. Thus, they can be used directly to determine the Hubble constant, H_0, and are also potential probes of the deceleration parameter q_0.

IC 4182 is the first galaxy for which the absolute magnitude of a SN Ia has been determined empirically by tying to the Cepheid distance scale. Preliminary results from observations made with the *Hubble Space Telescope* (*HST*) were announced in Sandage et al. (1992). The present paper discusses the *HST* data and its analysis, which leads to the Cepheid-based distance to IC 4182; the recalibration of the photometry for SN 1937C and thus the calibration of the peak absolute magnitude of SN 1937C in particular and SNe Ia in general; and the resulting estimate for H_0.

Detailed photometry and identification of the Cepheids (and other incidental variable stars) is presented, along with the special procedures employed to negotiate the peculiar data from the spherical-aberration–impaired *HST*. The mean colors of the Cepheids, the color-magnitude diagram of the brighter stars, and resolution of the tip of the old giant branch are presented and are used to evaluate the internal reddening/extinction needed for proper determination of the true distance to this galaxy.

2. OBSERVATIONS AND PRELIMINARY PROCESSING

Repeated images of a field in IC 4182 were taken with the Wide Field Camera (WFC) of the *HST* in the F555W passband. This 2.5 × 2.5 square field is shown in Figure 1 (Plate 1), superposed on a ground-based image of the whole galaxy. All the observations, spaced over a period of 47 days, were obtained at the same (telescope) orientation. The chosen field is rich in relatively bright resolved stars. A special timing scheme that eliminates aliasing problems in the period range 3 to 40 days was used to space the 20 exposures over the 47 day

[1] Data obtained with *HST* operated by AURA, under NASA Contract NAS5-26555.

[2] Affiliated to the Astrophysics Division, Space Sciences Department of ESA.

[3] Also, University of Catania, Italy.

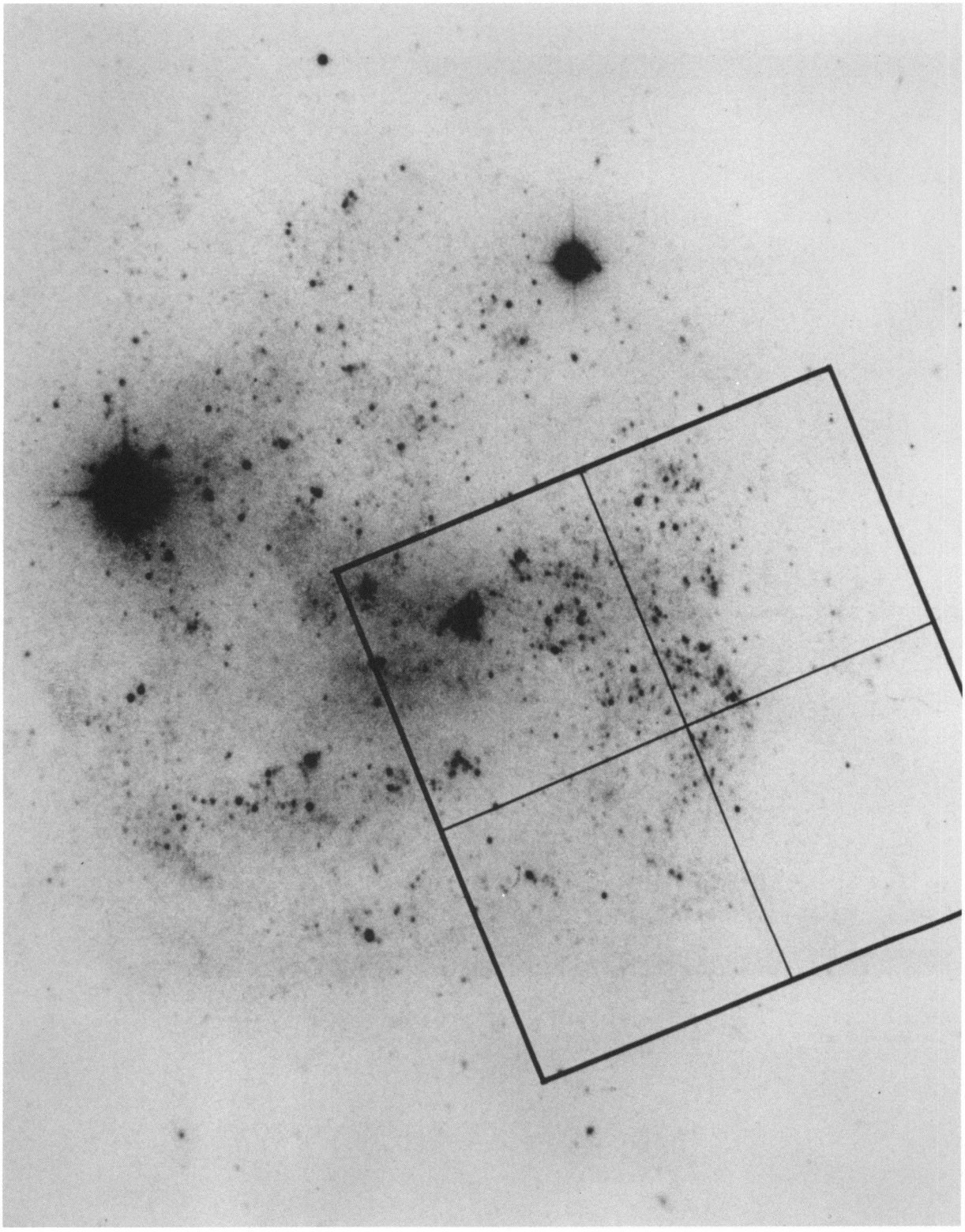

FIG. 1.—Reproduction of a ground-based image of IC 4182, showing the field observed by the WFC. The image is from a photograph made with the Palomar Hale 200 inch telescope.

TABLE 1

JOURNAL OF OBSERVATIONS

Data Archive Designation	HJD at Midexposure	Filter	Exposure Time (s)
W0UA0101T +... 02T	2448648.6631	F555W	3800
W0UA0201T +··· 02T	2448654.6982	F555W	4200
W0UA0301T +··· 02T	2448660.1283	F555W	4200
W0UA0303T +··· 04T	2448660.2623	F785LP	4200
W0UA0401T +··· 02T	2448662.6076	F555W	3300
W0UA0501T +··· 02T	2448664.5514	F555W	4200
W0UA0601T +··· 02T	2448667.0988	F555W	4200
W0UA0701T +··· 02T	2448667.5009	F555W	4200
W0UA0801T +··· 02T	2448668.1717	F555W	4200
W0UA0A01T +··· 02T	2448669.3787	F555W	4200
W0UA0B01T +··· 02T	2448670.1163	F555W	4200
W0UA0C01T +··· 02T	2448671.1218	F555W	4200
W0UA0D01T +··· 02T	2448671.3232	F555W	4200
W0UA0E01T +··· 02T	2448672.1281	F555W	4200
W0UA0F01T +··· 02T	2448673.2011	F555W	4200
W0UA0G01T +··· 02T	2448675.1484	F555W	4200
W0UA0H01T +··· 02T	2448677.0950	F555W	4200
W0UA0I01T +··· 02T	2448679.0408	F555W	4200
W0UA0I03T +··· 04T	2448679.1749	F785LP	4200
W0UA0J02T	2448684.2375	F555W	2100
W0UA0K01T +··· 02T	2448691.1064	F555W	4200
W0UA0L01T +··· 02T	2448694.7231	F555W	3800

window. Two equal exposures were taken at each epoch so that anticoincidence matching could be used to minimize the effect of cosmic-ray events. At 2 of the 20 epochs, additional exposures in the F785LP passband were also obtained. Table 1 lists the journal of observations and the *HST* data archive identifications.

Bias subtraction and flat-fielding were done in the standard Space Telescope Science Institute (STScI) data processing pipeline. Tests showed that these could not be significantly improved upon using available calibrations. It is important to note that during the 47 day period spanned by the observations, several decontamination procedures were tried on the WF/PC cameras: the sensitivity of the chips show variation of up to 0.15 mag with epoch, and the "measles" problem showed up to varying degrees, depending on epoch.

In the section on photometry, it will be shown how the effects from the first problem are eliminated, and that the second adds an uncertainty of photometry by 0.02 mag rms. Photometric reductions and detection of variable stars were performed independently by the coauthors at the STScI and those at the University of Basel and then compared. In the following sections the independent efforts are described.

3. PHOTOMETRY AND DETECTION OF VARIABLE STARS AT STScI

3.1. *Elimination of Cosmic Rays*

Examination of the individual exposures shows that cosmic rays severely contaminate the exposures. To bring this problem under some control, the back-to-back exposures were combined in the following way.

1. The pairs of images were averaged.
2. Individual pairs of corresponding pixels in the component images were compared, and the difference in their values was compared to the noise expected from the combined effect of the Poisson photon statistics and the readout noise. If this difference exceeded 5 σ, the value of the pixel in the output averaged image was replaced by the lower of the two values.

This procedure works only if the images are registered to better than 0.1 pixels, as the back-to-back images indeed are. Due to the severe undersampling, indiscriminate use of this procedure will end up truncating the peaks of the brighter stars and destroy photometric fidelity. Meticulous tests were performed to ensure that this did not happen.

The resulting combined images were used in all downstream photometry and analysis. For one of the epochs (W0UA0J02T in Table 1), the second component image is missing, and for this epoch the image was used as is. All mention of individual images hereafter will refer to those obtained from this pairwise combining procedure, unless specifically stated. While the above procedure removes cosmic rays above the 5 σ level (and for W0UA0J, not at all), the "fainter" cosmic rays and "hot pixels" remain and were dealt with during photometry with a different procedure.

A "template" image was constructed by co-adding images taken at five different epochs (so as to maximize the chance of including faint variables that might drop below the detection threshold of some individual images). The registration across images taken at different epochs is off by as much as 4 pixels, even though the back-to-back image pairs are superbly aligned. To overcome this problem while making the template image, *integer* pixel shifts were applied to assure the registration. While apparently better results can be obtained by fractional pixel alignment, such a procedure would necessitate interpolation of pixel values. Because of the severely undersampled stellar images on these pictures, this would severely compromise photometric fidelity. The stellar profiles in the template image are thus not as "sharp" as on the individual epochs, but photometric fidelity is not lost.

3.2. *Methodology for Photometry*

The photometry was performed independently at STScI and at Basel and by independent methods. At STScI, a *variant* of the DoPHOT program (Mateo & Schechter 1989; Schechter, Mateo, & Saha 1993) was used. Standard DoPHOT is normally used on well-sampled images that have Gaussian-like

stellar profiles. Several distinct problems appear for the current data and are handled as follows.

1. The stellar profiles are severely undersampled in the WFC data. DoPHOT fits profiles to the pixel values by assuming that the value corresponds to the center of the pixel. This is essentially tantamount to assuming that the profiles are piecewise linear across adjacent pixels. For undersampled images this is inadequate. The program was altered to integrate up to second-order terms in the model-profile across the face of each pixel. DoPHOT's use of analytical models presents a distinct advantage in carrying out such a procedure.

2. The form of the DoPHOT model profile is inadequate for describing the flared profiles from the spherical-aberration–impaired *HST*. The form of the analytic profile was augmented so that a suitable profile can be made good to 6 pixels from the stellar profile center. This model permits only elliptical isophotes, but as tests described below show, this works adequately.

3. The cosmic-ray events on WFC data are harder to distinguish from the cores of stellar profiles than in the case of well sampled ground-based data. Even so, visual inspection shows that such distinction is possible. The criteria used in DoPHOT were significantly altered so that the residual cosmic rays (left over from the combining procedure described in § 3.1) can be identified. This is crucial if reliable photometry is to be obtained.

4. The halos of the WFC stellar point-spread function (PSF) have complicated structure, with tendrils and rings. Since these structures are low-level, the elliptical model analytic PSF still works. The structures themselves are elongated and cannot be confused with stars. However, the intersection points of such structures can be mistaken for stars. The problem is to prevent DoPHOT from triggering on these structures. Fortunately, these features have much lower contrast than the cores of stellar PSFs. A sufficiently high-pass spatial filter, specifically a 5×5 pixel median filter, lets all the stellar PSFs through but blocks detection of the substructure around the brighter stars. It should be emphasized that this filter is used only for finding stars, and all subsequent photometry is done on the unfiltered image.

5. In standard use, DoPHOT is used to fit the analytic profile relatively far out into the wings, and the signal-to-noise ratios S/N's of individual pixels are used for weights. This is impractical for the *HST* images for several reasons. As one goes far from the image core, the structure becomes increasingly difficult to describe with an analytic function. In any case, for all except the brightest stars, the far halo regions contribute more noise than signal. Fitting was restricted to an 11×11 pixel subraster about the central pixel for each star. The analytic functional PSF model was so adjusted that it is insignificantly different from zero 10 pixels away from the star center. The *actual* PSF halo falls off much more slowly, so the effect of this procedure is to fit the rise of the *core* of the star above its own halo. Measured in this way, the ratio of fluxes between two stars on the same frame (or relative magnitudes) is preserved.

We are indebted to P. Schechter for many discussions regarding the above modifications and for supplying the algorithm that performs the integration over the pixel face. However, the responsibility for any errors or shortcomings lies solely with us.

Reported DoPHOT magnitudes represent the "height" of the fitted PSF. For the same star, this differs from image to image depending on the PSF changes due to spacecraft jitter, focus changes, and the like. However, relative differences in magnitudes on the same image are preserved *as long as the PSF is invariant across the field*, and DoPHOT reported magnitudes for corresponding stars differ from image to image by a zero-point additive term:

$$m'_i(r) = m'_j(r) + C'_{ij}(r) , \quad (1)$$

where $m'_i(r)$ is the DoPHOT reported magnitude for any given star r on the ith image. It is seen that the values of $C'_{ij}(r)$ for all the various stars on the two images scatter by 0.04 mag rms (except at the very faint end, where Poisson photon statistics drive larger errors), so the average over r, i.e., $C'_{ij} = \langle C'_{ij}(r) \rangle$ is the systemic difference of DoPHOT magnitudes between the i and j images. Recall that all images were taken in the same telescope position and orientation, so this comparison is unaffected by the field dependence of the PSF.

While it is well known that the PSF varies across the WFC field, the scheme described above fits only the cores, which is the part of the PSF that varies least. The consequences of proceeding with the assumption that the PSF appears invariant to the DoPHOT fitting scheme described above were examined empirically. The altered version of DoPHOT was pretested on images of the LMC cluster NGC 1850 taken during science verification of the WFC. Two sets of images were available, taken with different positioning and orientation: there were many stars in common on the two sets, but any given star was moved in position by typically 300 pixels. The DoPHOT magnitudes from set A were compared to those from set B after allowing for a zero-point shift as discussed above. By restricting the comparison to only those stars where the predicted *random* errors in measurement are less than 0.030 mag rms (implying that the expected scatter in the difference for corresponding stars is 0.042 mag rms), we find that there is agreement to 0.070 mag rms. This implies that the combined effect of flat-field uncertainties (of order 3%) and PSF variations is contained within 0.07 mag rms. By fitting a slowly varying polynomial as a function of star position to attempt to model out the PSF variation, the scatter can be reduced formally to 0.058 mag rms. This experiment thus substantiates the claim that fitting a core PSF in the manner described above yields relative magnitudes across a given camera chip that are systematically good to 0.07 mag *without* the need for any further adjustment. Comparing repeat observations of the same field where the stars are placed in the same position (to within a few pixels) shows that the DoPHOT magnitudes scatter by only the *predicted* uncertainty, an estimate made by DoPHOT based on the noise model using read noise and Poisson photon count statistics. These conclusions play a central role in the adopted procedure for finding and measuring the variable stars as discussed below.

Tests were also done to estimate the scatter introduced by the so called "measles" problem, which is believed to be caused by nonuniform condensation of contaminants on the windows in front of each CCD chip of the WF/PC. The flat field images reveal spots (measle-like) a few pixels across, with apparent sensitivity reduced by typically 2%–3% in F555W. The effect of the contaminants and the "measles" are more severe in the blue and particularly in the ultraviolet. A detailed description of this problem and the efforts to deal with it is given in Mackenty et al. (1993). The concern was whether the attenuation caused by these features for stars is the same as for the flat field, particularly given that the windows bearing the

contaminants are very close to the chips (and hence the focus). The most measles-free and most measles-affected images of the IC 4182 data set were processed using the method above and compared. The scatter (in the difference) for the stars with predicted S/N greater than 30 was found to be 0.05 mag rms. Recall that the stars are repositioned at the same location on the respective chips. These results show that

(1) for the same star, the image-to-image uncertainty is the larger of $0.05/2^{1/2}$, or the DoPHOT predicted error estimate, and

(2) the star-to-star scatter in magnitude determination on the same image is ≈ 0.07 mag and essentially governed by flat-fielding uncertainty and PSF variation and only *insignificantly* by the measles problem.

3.3. *Calibrating the Photometry*

The DoPHOT variant method was used to derive m'_i (following the notation above) for all possible stars on all the individual images. Each of the four chips were treated separately, since the PSFs differ due to the separate reimaging cameras. Similar reductions were also performed for the "template" image, to obtain m'_t for all discernible stars. Only those objects that were classified unambiguously as stars by DoPHOT were considered in all further analysis. Each star found on the template was matched to the same star on all the individual epochs. However, sometimes a star on the template cannot be found in a given individual image because it is too faint, etc., and so cannot be used in further analysis. Let us say that n matches are made for the ith image. For the rth matched star we have

$$m'_t(r) - m'_i(r) = C'_{ti} . \quad (2)$$

If star r is not variable, and since all images are registered to within a few pixels, the above equation yields C'_{ti} to an uncertainty of 0.05 mag rms. In practice, there are several hundred stars on each of the four chips with m' determined with S/N greater than 20, and the ensemble average yields a very accurate determination of C'_{ti}, to better than 0.01 mag rms and effectively eliminates errors from the relatively few variable stars. Thus, for the ith image, each star r can be transformed to the system of the template, where this template-referred magnitude $m^t_i(r)$ is given by

$$m^t_i(r) = m'_i(r) + C'_{ti} . \quad (3)$$

The template-referred magnitudes differ from the true magnitudes by an additive constant (one for each chip, since each chip is treated independently through the above process). In order to evaluate this, three to eight suitably bright isolated stars on each chip on the F555W image in the third epoch were measured with an aperture of radius 4″, which is large enough to include all the light. The third epoch was chosen, since it was timed immediately following a decontamination procedure, and the instrumental response most closely adheres to that represented by the standard flat field used in the calibrations, as shown by the so called internal "delta" flats in the calibration archives.

The calibration of the integrated DN (data numbers) from a star as measured in a 4″ aperture is related to the standard F555W magnitudes by Table 12.15 of Hunter et al. (1922, hereafter the SV Report). Thus the additive shift needed to go from m^t_3 to true F555W magnitudes (m_3) were evaluated for each chip, using a few suitably bright and relatively isolated stars. Note that the same additive shift also corrects m^t_i to true F555W magnitudes m_i. In two of the sparser chips (i.e., areas where the star density is low), concordance between the various measured stars was within 0.05 mag. On the two chips where the crowding is more severe, truly isolated bright stars are not present, and contamination within the 4″ aperture or in the "sky" aperture by faint stars produces additional scatter. Extreme differences between stars were as large as 0.4 mag, but in the mean the additive correction could be evaluated to 0.1 mag. The same procedure was also used to obtain the corrected F785LP magnitudes.

As a check on the F555W measurements, a ground-based image in V of IC 4182, obtained by Kristian and Carlson with the COSMIC camera at the prime focus of the 200 inch Hale telescope, was examined. Standard DoPHOT was run on this image. This image has a much bigger field, and stars on the outer parts well away from the galaxy could be used to calibrate the zero point in the usual way. The calibrated DoPHOT fitted V magnitudes for the same stars used to calibrate the true F555W magnitudes were now determined. These V magnitudes suffer also from several crowding problems and agree only to 0.15 mag with the F555W magnitudes obtained above (the color and zero-point terms between the V and F555W system introduce differences only to a few hundredths of a magnitude; (see Harris et al. 1991), but they are good enough to endorse our erstwhile calibration. Similarly, the step-scale V magnitude calibration on 200 inch primary focus plates (Sandage & Tammann 1982) were found to be in agreement to 0.2 mag.

3.4. *Finding Variables and Determining Light Curves*

Armed with calibrated photometry in F555W at each epoch, and with each star detected on the template matched to the same star whenever detected on each individual epoch, the search for variables was done using essentially the method described in Saha & Hoessel (1990). Recall from the previous discussion that for any given star the formal uncertainty in the magnitude difference on two different epochs can be derived from the DoPHOT reported measurement errors; there is no additional uncertainty. However, *all* measurements of the same object on different epochs suffer from an identical systematic uncertainty of up to 0.1 mag.

The search for variables was made using a χ^2 test, followed by a "periodicity" test based on a variant of the Lafler & Kinman (1965) algorithm. This technique has been demonstrated in Saha & Hoessel (1990). The DoPHOT estimated errors are the appropriate input for the χ^2 test. Objects with χ^2_ν (reduced χ^2) greater than 8 were always flagged as possible variables. Objects shown as variables at the 99% confidence level, but $\chi^2_\nu \leq 8$, were tested for periodicity (using the Λ statistic as described in Saha & Hoessel 1990), and those with periodicity goodness statistic $\Lambda \geq 3.5$ (in the period search range 3 to 50 days) were also flagged as possible variables.

All the candidates selected by the above process were visually inspected for variability by "blinking" on a video display for confirmation, to weed out specious candidates (these arise as a result of image pathologies and non-Gaussian sources of error, as discussed in detail in Saha & Hoessel 1990). A total of 38 bona fide variables (not necessarily Cepheids) were found. These are identified in Figure 2 (Plates 2–5). Figure 3 (Plate 6) shows two of the variables as they appear visually on their respective maximum and minimum apparitions. The F555W magnitude obtained for each of these objects at each phase from the STScI photometry is listed in Table 2. An additional object, C3-V12 was identified by the

PLATE 2

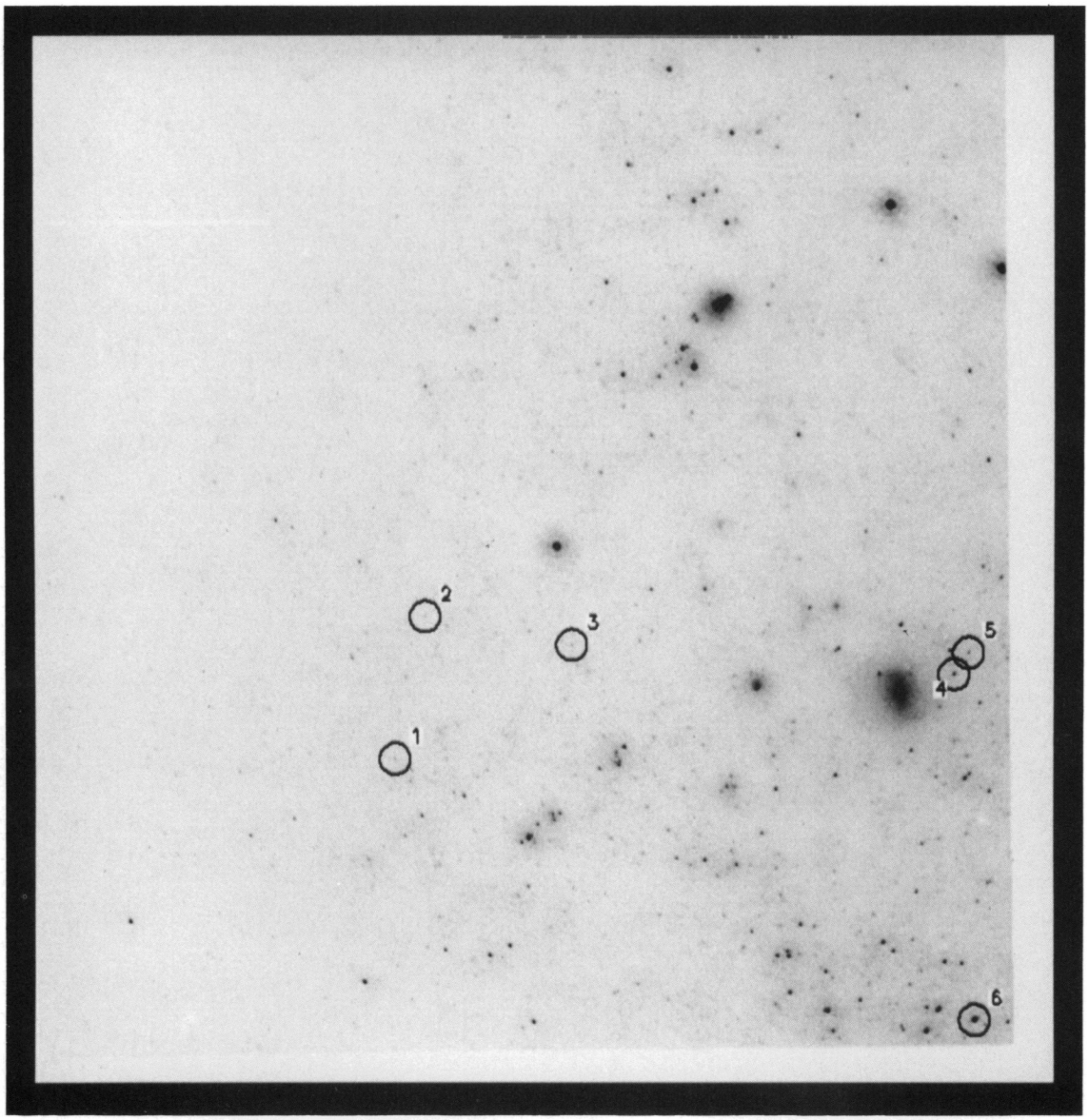

FIG. 2*a*

FIG. 2.—(*a*) Finding chart for variables on chip 1. Orientation is *not* along cardinal directions. Objects indicated are at the very centers of the marked circles. Object marked "*n*" should be read as "C1-Vnn." (*b*) Same as above but for chip 2. Object marked "*n*" should be read as "C2-Vn." (*c*) Same as above but for chip 3. Object market "*n*" should be read as "C3-V*n*"; C3-V12 is out of sequence. (*d*) Same as above but for chip 4. Object marked "*n*" should be read as "C4-V*n*."

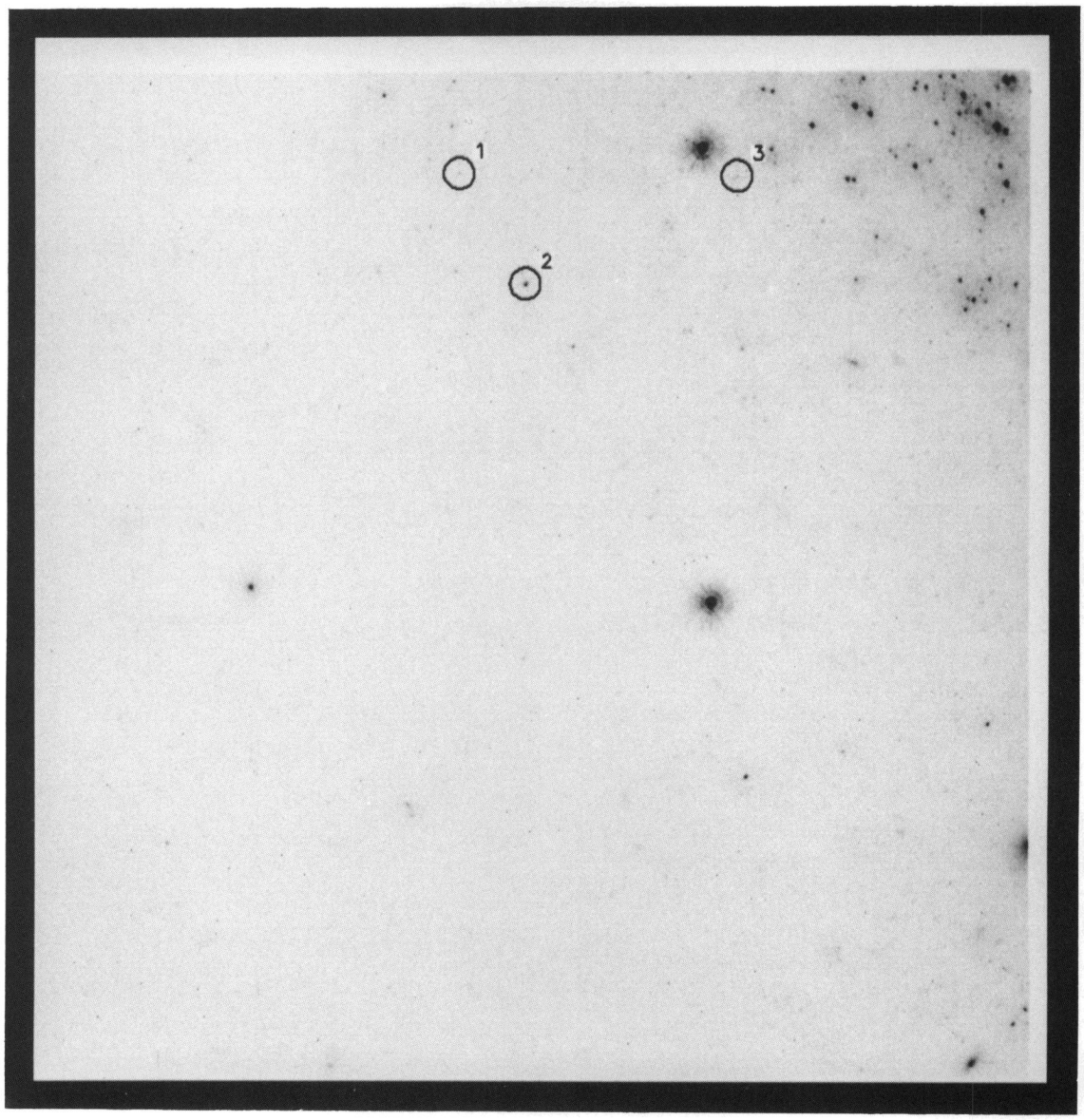

FIG. 2*b*

SAHA et al. (see 425, 17)

PLATE 4

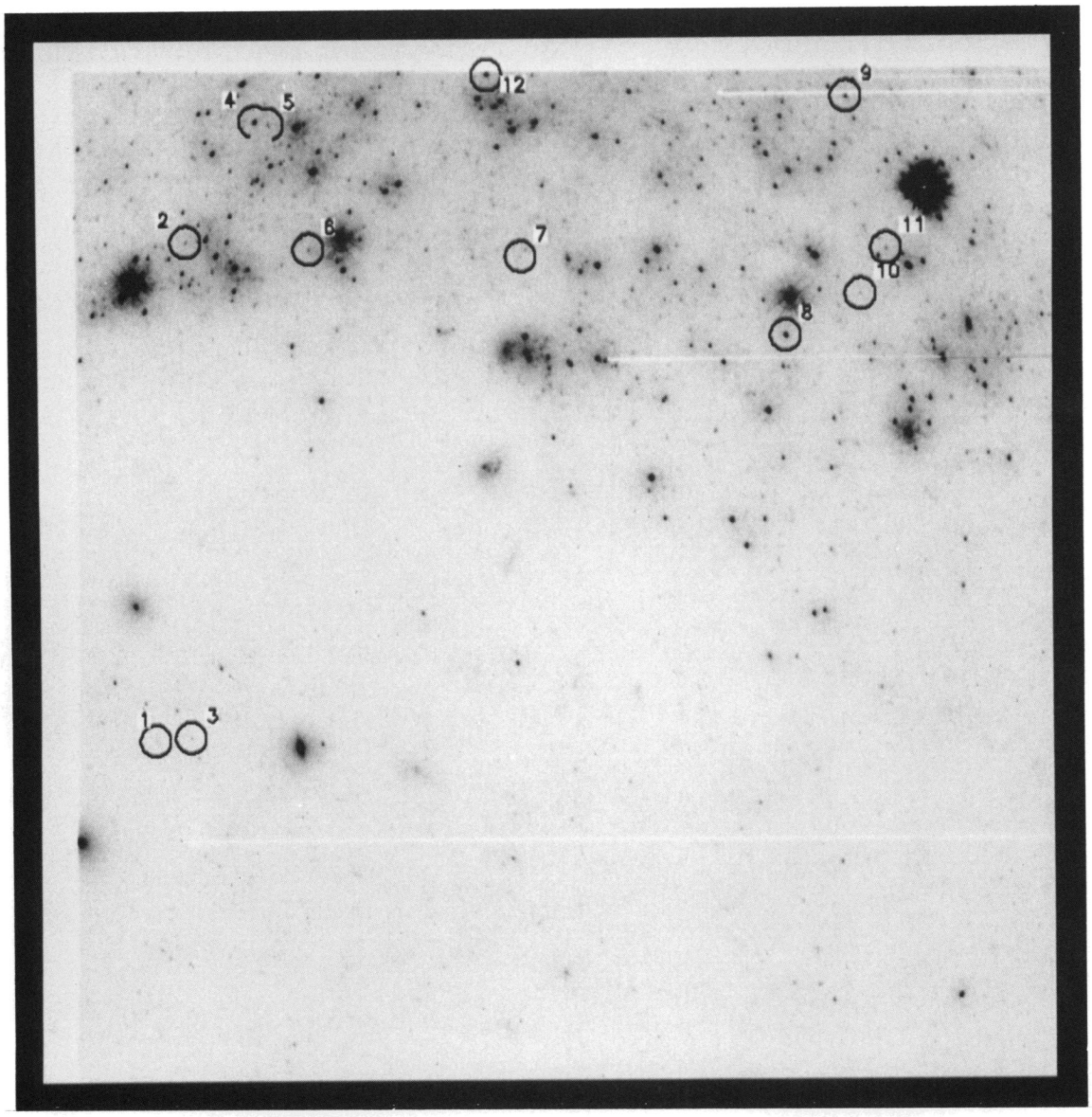

FIG. 2*c*

SAHA et al. (see 425, 17)

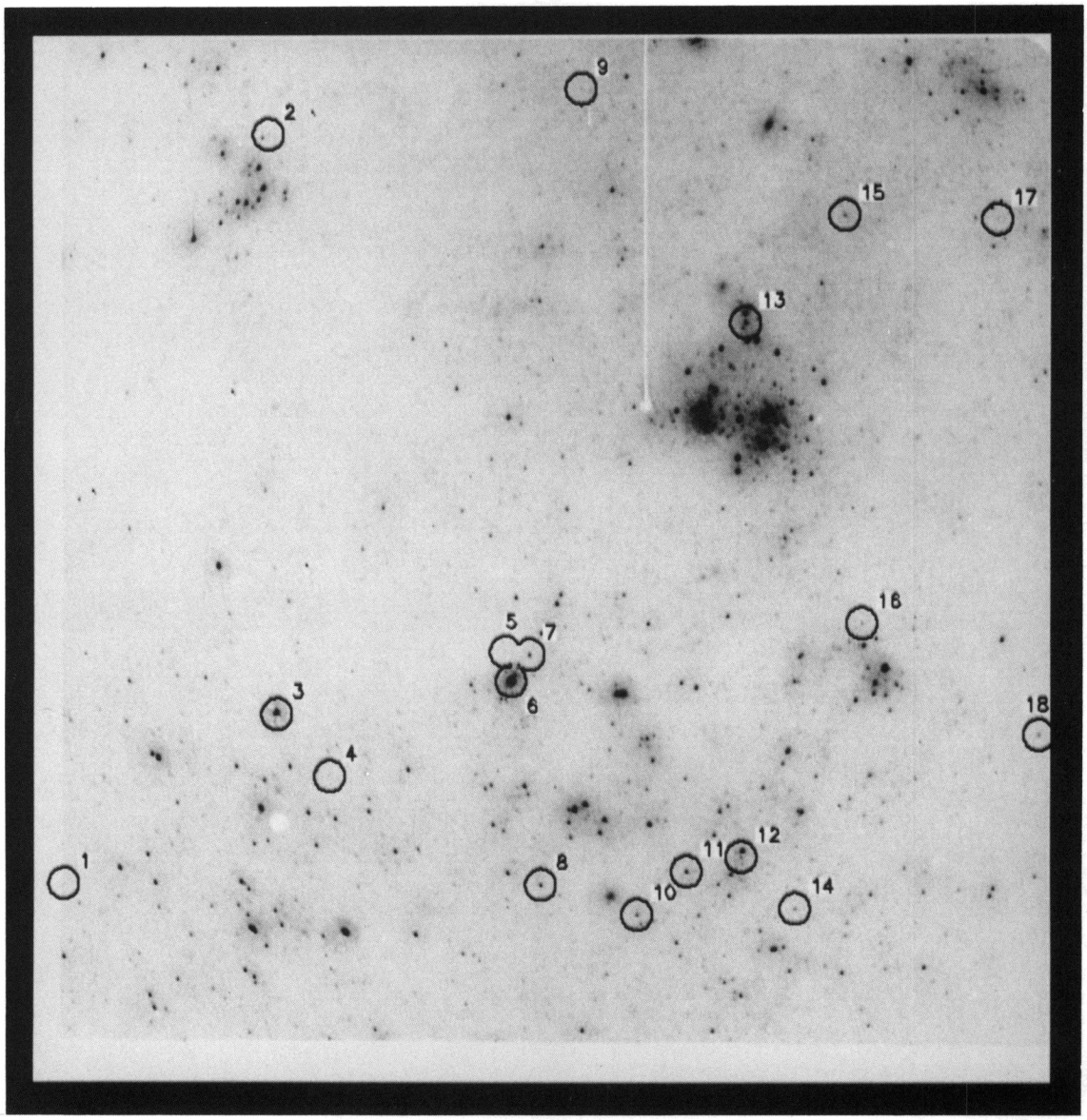

FIG. 2*d*

SAHA et al. (see 425, 17)

PLATE 6

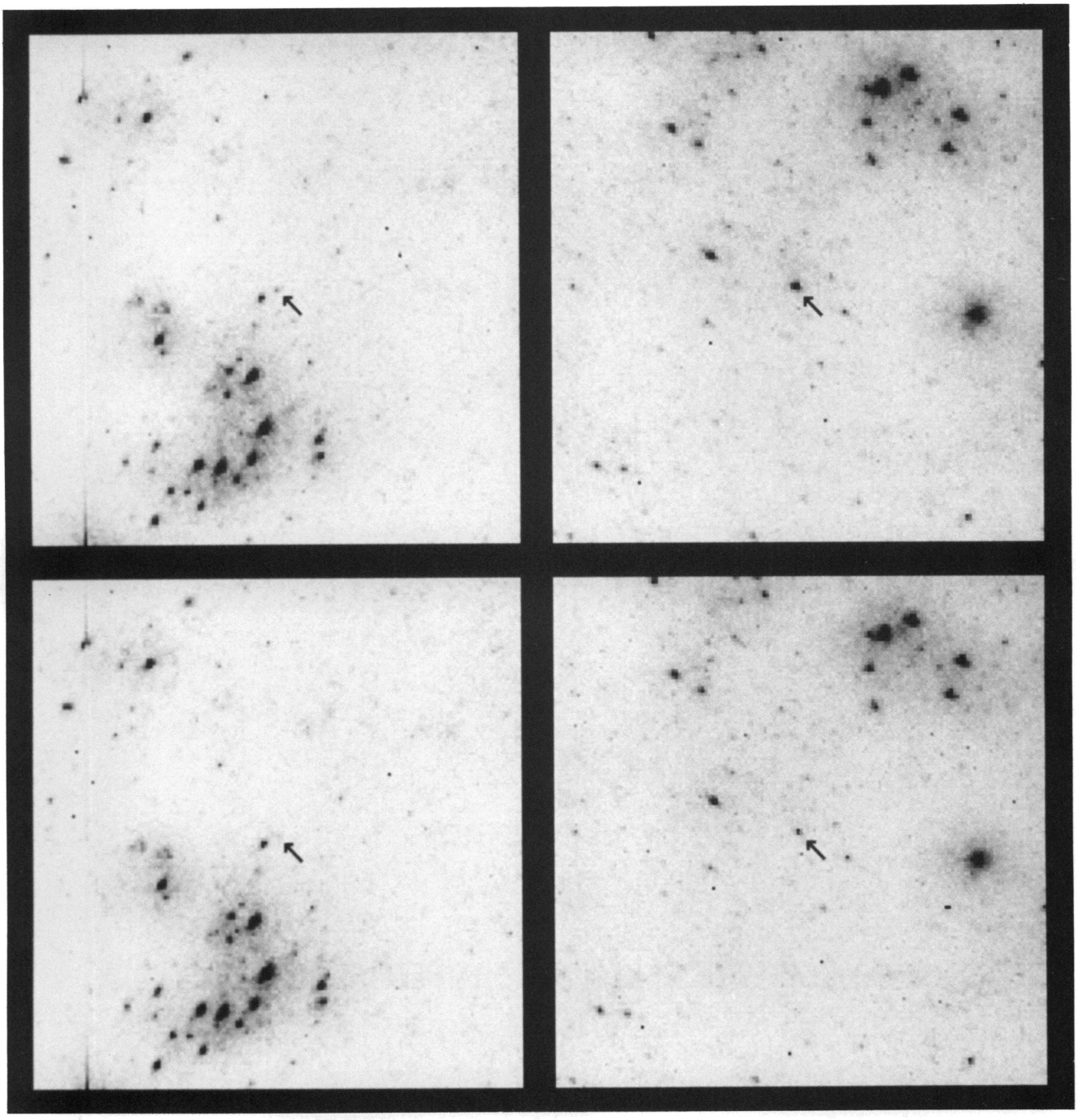

FIG. 3.—Enlarged display of the area around the variables C4-V1 (*left panels*) and C4-V8 (*right panels*) showing each of these objects at intensity extrema

TABLE 2

PHOTOMETRY OF VARIABLE STARS: MAGNITUDES AND ERROR ESTIMATES

HJD	C1–V1	C1–V2	C1–V3	C1–V4	C1–V5	C1–V6	C2–V1	C2–V2
2448648.6632	24.42 0.10	25.11 0.16	24.63 0.11	23.40 0.05	24.58 0.12	22.00 0.03	24.44 0.09	22.91 0.03
2448654.6982	24.30 0.10	24.58 0.10	24.55 0.09	23.82 0.07	24.35 0.09	22.20 0.03	24.48 0.09	23.13 0.04
2448660.1284	24.08 0.06	24.27 0.07	24.49 0.10	23.85 0.06	23.76 0.06	22.38 0.03	24.77 0.10	23.30 0.04
2448660.262*	23.73 0.08	23.51 0.07	...	22.68 0.06	23.39 0.07	21.35 0.04	23.74 0.08	21.96 0.05
2448662.6077	24.40 0.10	24.83 0.12	24.65 0.14	22.90 0.03	24.13 0.08	22.50 0.03	25.24 0.18	23.44 0.04
2448664.5515	24.77 0.11	25.09 0.14	24.48 0.10	22.89 0.04	24.46 0.10	22.58 0.03	24.41 0.07	23.47 0.04
2448667.0988	24.30 0.10	24.27 0.08	24.57 0.08	23.08 0.04	24.63 0.11	22.58 0.03	24.74 0.12	23.18 0.03
2448667.5009	24.28 0.09	24.38 0.07	24.35 0.09	23.11 0.04	24.11 0.06	22.52 0.04	24.99 0.14	23.13 0.04
2448668.1718	24.46 0.10	24.45 0.08	24.26 0.08	23.15 0.04	23.91 0.06	22.48 0.04	25.15 0.15	23.05 0.04
2448669.3788	24.49 0.09	24.83 0.12	24.41 0.09	23.20 0.04	23.86 0.06	22.10 0.03	25.03 0.13	22.80 0.03
2448670.1163	24.46 0.16	24.92 0.12	24.76 0.13	23.23 0.05	23.81 0.06	21.88 0.03	24.51 0.08	22.70 0.03
2448671.1219	24.85 0.14	...	24.95 0.15	23.27 0.05	23.88 0.06	21.58 0.03	24.40 0.09	22.59 0.03
2448671.3233	24.70 0.12	24.97 0.13	24.93 0.12	23.32 0.05	23.93 0.06	21.53 0.03	24.42 0.07	22.59 0.03
2448672.1282	24.57 0.11	24.97 0.14	24.92 0.12	23.34 0.05	24.19 0.07	21.43 0.03	24.56 0.08	22.56 0.03
2448673.2011	24.33 0.10	24.28 0.06	24.83 0.13	23.43 0.05	24.40 0.09	21.36 0.03	24.92 0.12	22.56 0.03
2448675.1484	24.35 0.08	24.41 0.07	24.90 0.14	23.58 0.06	24.63 0.11	21.45 0.03	24.95 0.12	22.64 0.03
2448677.0950	24.56 0.11	24.78 0.12	24.90 0.13	23.74 0.06	24.18 0.09	21.53 0.03	24.55 0.09	22.70 0.04
2448679.0409	24.83 0.13	25.20 0.15	25.22 0.16	23.81 0.06	23.85 0.06	21.60 0.03	24.80 0.10	22.71 0.03
2448679.175*	23.80 0.08	24.09 0.10	...	22.60 0.06	23.35 0.07	20.94 0.04	23.89 0.08	21.57 0.05
2448684.2376	...	...	24.49 0.10	23.73 0.09	24.55 0.12	21.71 0.07	24.69 0.15	22.91 0.04
2448691.1064	24.78 0.13	24.44 0.08	24.50 0.08	23.05 0.04	24.33 0.09	22.03 0.03	25.00 0.11	23.11 0.03
2448694.7231	24.09 0.09	24.60 0.09	24.49 0.09	23.18 0.04	24.43 0.09	22.10 0.03	24.73 0.10	23.23 0.04

HJD	C2–V3	C3–V1	C3–V2	C3–V3	C3–V4	C3–V5	C3–V6	C3–V7
2448648.6632	...	...	24.13 0.09	25.30 0.19	22.22 0.04	24.76 0.17	24.31 0.12	24.94 0.18
2448654.6982	25.23 0.17	24.59 0.10	23.81 0.07	24.72 0.12	22.30 0.03	24.14 0.09	23.76 0.07	25.00 0.17
2448660.1284	25.02 0.14	25.06 0.14	24.42 0.10	24.73 0.12	22.35 0.03	24.50 0.12	23.86 0.07	24.67 0.11
2448660.262*	23.69 0.08	24.76 0.12	24.97 0.12	...	...	...	...	24.32 0.11
2448662.6077	24.94 0.16	24.63 0.12	24.43 0.12	24.63 0.11	22.40 0.04	24.25 0.13	23.78 0.07	25.32 0.24
2448664.5515	24.46 0.09	25.08 0.16	24.36 0.10	24.43 0.08	22.41 0.03	24.14 0.09	24.57 0.17	25.48 0.23
2448667.0988	24.80 0.12	24.55 0.09	24.24 0.09	24.11 0.08	22.40 0.04	25.01 0.19	24.32 0.09	...
2448667.5009	24.81 0.12	24.64 0.09	23.98 0.08	24.50 0.09	22.46 0.03	24.74 0.13	23.90 0.07	24.94 0.16
2448668.1718	25.07 0.14	24.99 0.12	24.08 0.08	24.31 0.08	22.48 0.03	24.61 0.12	23.74 0.07	24.85 0.13
2448669.3788	24.80 0.12	25.38 0.19	24.14 0.08	24.39 0.08	22.48 0.04	24.52 0.13	23.84 0.06	25.39 0.20
2448670.1163	24.24 0.08	25.52 0.22	24.03 0.07	24.90 0.23	22.51 0.04	24.61 0.16	23.91 0.06	25.69 0.28
2448671.1219	24.31 0.08	24.55 0.09	25.23 0.19	24.30 0.08	22.47 0.03	24.80 0.20	24.14 0.09	...
2448671.3233	24.31 0.10	24.86 0.10	24.49 0.12	24.28 0.08	22.46 0.03	24.32 0.13	23.91 0.06	25.68 0.29
2448672.1282	24.64 0.10	24.86 0.13	23.95 0.08	...	22.51 0.04	24.25 0.09	23.88 0.07	25.32 0.18
2448673.2011	24.68 0.12	...	24.60 0.12	24.33 0.09	22.50 0.03	24.88 0.24	23.72 0.07	24.91 0.14
2448675.1484	24.93 0.13	25.02 0.14	24.51 0.12	24.30 0.08	22.51 0.04	24.92 0.18	24.05 0.09	25.13 0.17
2448677.0950	24.20 0.08	25.13 0.14	24.23 0.09	24.28 0.08	22.55 0.03	23.99 0.08	23.75 0.06	25.61 0.23
2448679.0409	24.51 0.10	...	24.09 0.09	24.15 0.08	22.56 0.04	...	24.14 0.09	24.55 0.11
2448679.175*	24.11 0.10	24.72 0.11	...	...	...	...	...	24.71 0.12
2448684.2376	24.27 0.11	24.74 0.13	...	24.18 0.09	22.68 0.04	...	24.30 0.11	...
2448691.1064	24.15 0.08	...	24.19 0.09	23.95 0.05	22.71 0.04	24.11 0.10	23.85 0.07	24.77 0.13
2448694.7231	24.93 0.13	25.11 0.17	24.30 0.10	23.98 0.06	22.70 0.04	24.82 0.19	24.28 0.10	25.41 0.23

HJD	C3–V8	C3–V9	C3–V10	C3–V11	C3–V12	C4–V1	C4–V2	C4–V3
2448648.6632	22.33 0.04	23.85 0.18	24.34 0.10	24.01 0.08	22.39 0.05	24.55 0.12	24.55 0.10	21.51 0.05
2448654.6982	22.18 0.04	22.58 0.04	25.19 0.18	23.85 0.07	22.54 0.05	25.55 0.29	24.60 0.12	21.56 0.05
2448660.1284	22.38 0.04	22.63 0.04	24.40 0.10	24.03 0.07	22.63 0.05	24.75 0.12	24.47 0.08	21.13 0.05
2448660.262*	...	22.26 0.05	23.50 0.07	23.00 0.07	21.45 0.05	23.26 0.07	24.63 0.11	...
2448662.6077	22.43 0.05	22.80 0.04	24.76 0.15	24.23 0.10	22.29 0.05	24.88 0.19	24.89 0.17	...
2448664.5515	22.49 0.10	22.92 0.04	24.91 0.12	24.39 0.09	22.06 0.05	25.02 0.16	25.31 0.18	21.14 0.05
2448667.0988	22.31 0.04	23.13 0.05	24.66 0.11	24.38 0.11	21.97 0.05	24.38 0.11	24.53 0.10	21.13 0.05
2448667.5009	22.28 0.04	23.17 0.04	24.83 0.11	24.03 0.08	21.92 0.05	24.64 0.12	24.70 0.11	21.13 0.05
2448668.1718	22.21 0.04	23.22 0.05	24.53 0.10	24.34 0.09	21.90 0.05	25.07 0.17	24.59 0.09	21.11 0.05
2448669.3788	22.13 0.04	23.19 0.05	24.26 0.09	23.99 0.07	21.94 0.05	...	25.03 0.18	21.24 0.05
2448670.1163	22.05 0.04	23.26 0.05	24.34 0.08	23.67 0.06	21.88 0.05	24.36 0.10	24.91 0.15	21.10 0.05
2448671.1219	...	23.20 0.05	24.39 0.08	23.72 0.06	21.92 0.05	24.72 0.14	25.17 0.22	21.15 0.05
2448671.3233	22.09 0.04	23.17 0.04	24.39 0.09	23.80 0.06	21.91 0.05	...	24.77 0.12	21.20 0.05
2448672.1282	22.02 0.04	23.10 0.05	24.47 0.09	23.77 0.06	21.93 0.05	24.85 0.16	24.60 0.10	21.19 0.05
2448673.2011	22.19 0.04	23.19 0.04	24.57 0.09	23.93 0.07	21.97 0.05	25.09 0.15	24.67 0.12	21.16 0.05
2448675.1484	22.28 0.04	23.05 0.05	24.88 0.11	24.02 0.07	22.04 0.05	24.96 0.16	25.13 0.16	21.16 0.05
2448677.0950	22.32 0.04	22.34 0.04	24.81 0.14	24.39 0.09	22.04 0.05	25.30 0.23	24.75 0.13	21.18 0.05
2448679.0409	22.35 0.04	22.44 0.04	24.40 0.09	24.49 0.10	22.07 0.05	25.08 0.18	24.73 0.11	21.13 0.05
2448679.175*	...	22.39 0.05	23.70 0.08	23.52 0.08	21.02 0.04	23.40 0.07	24.09 0.10	...
2448684.2376	22.39 0.04	22.75 0.05	...	23.80 0.08	...	...	24.50 0.11	21.84 0.20
2448691.1064	22.13 0.04	...	24.30 0.08	24.67 0.12	22.61 0.05	...	24.66 0.12	21.30 0.05
2448694.7231	22.31 0.04	...	24.85 0.13	24.18 0.09	22.69 0.05	...	24.80 0.13	21.18 0.05

TABLE 2—*Continued*

HJD	C4–V4	C4–V5	C4–V6	C4–V7	C4–V8	C4–V9	C4–V10	C4–V11
2448648.6632.....	24.89 0.16	25.47 0.26	20.71 0.03	22.66 0.04	23.19 0.05	24.39 0.11	22.70 0.03	22.03 0.03
2448654.6982.....	25.26 0.16	25.19 0.19	20.60 0.03	22.42 0.03	23.45 0.05	25.13 0.20	23.32 0.05	22.25 0.03
2448660.1284.....	...	24.94 0.13	20.57 0.02	22.63 0.03	22.69 0.03	24.81 0.15	23.68 0.06	22.44 0.03
2448660.262*.....	24.60 0.11	25.24 0.20	...	21.51 0.05	21.92 0.05	24.15 0.09	22.83 0.06	21.31 0.05
2448662.6077.....	24.61 0.13	25.26 0.22	20.52 0.03	22.69 0.04	22.38 0.03	25.02 0.18	23.48 0.07	22.45 0.03
2448664.5515.....	25.14 0.16	24.86 0.12	20.48 0.03	22.81 0.04	22.40 0.03	24.24 0.08	22.96 0.03	22.58 0.03
2448667.0988.....	24.48 0.10	25.64 0.26	20.34 0.02	22.86 0.04	22.50 0.04	24.57 0.13	22.80 0.03	23.23 0.21
2448667.5009.....	24.72 0.13	25.38 0.22	20.38 0.03	22.86 0.04	22.53 0.03	24.99 0.17	22.90 0.04	22.63 0.04
2448668.1718.....	24.91 0.14	24.63 0.10	20.35 0.03	22.86 0.03	22.50 0.03	24.95 0.16	22.92 0.03	22.66 0.04
2448669.3788.....	24.88 0.13	24.74 0.13	...	22.96 0.04	22.55 0.04	25.07 0.16	23.05 0.05	22.68 0.03
2448670.1163.....	25.26 0.19	25.35 0.19	20.31 0.02	22.97 0.04	22.63 0.04	24.77 0.12	23.11 0.04	22.80 0.03
2448671.1219.....	25.14 0.19	25.43 0.21	20.30 0.02	23.00 0.03	22.69 0.04	24.24 0.10	23.21 0.05	22.83 0.04
2448671.3233.....	25.02 0.16	...	20.32 0.03	23.05 0.04	22.65 0.03	24.31 0.10	23.21 0.04	22.78 0.04
2448672.1282.....	24.45 0.11	...	20.30 0.05	23.05 0.04	22.68 0.03	24.60 0.10	23.26 0.05	22.95 0.05
2448673.2011.....	24.70 0.12	24.85 0.14	20.30 0.03	23.10 0.04	22.72 0.03	24.69 0.14	23.36 0.04	22.88 0.04
2448675.1484.....	25.11 0.17	25.52 0.26	20.31 0.03	23.14 0.04	22.77 0.04	25.00 0.19	23.57 0.04	22.89 0.04
2448677.0950.....	24.40 0.09	24.74 0.12	20.30 0.03	23.32 0.05	22.85 0.03	24.74 0.14	23.56 0.04	22.99 0.04
2448679.0409.....	24.89 0.13	...	20.32 0.04	23.28 0.04	22.94 0.03	24.47 0.11	23.58 0.05	23.10 0.04
2448679.175*.....	24.54 0.11	...	...	22.07 0.05	21.93 0.05	24.33 0.10	23.03 0.07	21.74 0.05
2448684.2376.....	...	...	20.26 0.03	22.75 0.04	23.15 0.04	...	22.60 0.04	22.22 0.04
2448691.1064.....	25.10 0.17	24.93 0.16	20.27 0.02	22.38 0.03	23.46 0.05	24.44 0.10	23.25 0.04	22.08 0.03
2448694.7231.....	24.90 0.16	24.51 0.11	20.22 0.02	22.52 0.04	22.80 0.04	24.80 0.16	23.71 0.06	...

HJD	C4–V12	C4–V13	C4–V14	C4–V15	C4–V16	C4–V17	C4–V18
2448648.6632.....	23.53 0.06	22.97 0.04	23.39 0.04	23.34 0.06	23.88 0.08	24.82 0.19	23.05 0.04
2448654.6982.....	23.57 0.05	22.78 0.04	23.73 0.05	23.71 0.07	24.05 0.08	24.66 0.13	23.30 0.05
2448660.1284.....	24.18 0.10	24.84 0.03	23.86 0.05	23.90 0.08	23.53 0.05	24.59 0.12	23.66 0.06
2448660.262*.....	...	...	22.71 0.06	22.39 0.05	22.71 0.06	23.91 0.08	22.28 0.05
2448662.6077.....	23.44 0.08	22.68 0.07	23.65 0.06	23.88 0.09	23.69 0.06	24.65 0.14	23.46 0.06
2448664.5515.....	23.55 0.05	23.34 0.05	23.15 0.03	23.30 0.05	23.91 0.06	24.91 0.15	23.63 0.05
2448667.0988.....	24.05 0.09	...	23.20 0.04	23.44 0.07	24.14 0.09	24.92 0.17	23.65 0.05
2448667.5009.....	23.52 0.05	22.95 0.04	23.20 0.04	23.35 0.05	24.14 0.08	24.64 0.12	23.58 0.05
2448668.1718.....	23.90 0.06	22.84 0.03	23.30 0.04	23.32 0.05	24.23 0.09	24.59 0.11	23.63 0.06
2448669.3788.....	23.60 0.05	22.77 0.04	23.38 0.04	23.46 0.06	24.15 0.07	24.52 0.10	23.51 0.05
2448670.1163.....	24.07 0.09	22.99 0.07	23.35 0.04	23.43 0.06	24.27 0.09	24.58 0.14	23.38 0.05
2448671.1219.....	23.97 0.08	23.24 0.04	23.38 0.04	23.48 0.05	24.17 0.07	24.88 0.14	23.16 0.04
2448671.3233.....	23.59 0.06	23.32 0.05	23.40 0.05	23.45 0.05	24.11 0.09	25.05 0.17	23.17 0.04
2448672.1282.....	...	22.77 0.03	23.51 0.05	23.61 0.05	24.02 0.07	25.19 0.20	23.06 0.04
2448673.2011.....	23.80 0.06	22.75 0.03	23.52 0.05	23.69 0.05	23.35 0.04	25.43 0.24	22.96 0.04
2448675.1484.....	23.78 0.06	23.06 0.07	23.70 0.05	23.63 0.06	23.47 0.05	24.56 0.12	23.02 0.04
2448677.0950.....	23.98 0.09	...	23.86 0.06	23.91 0.07	23.60 0.05	24.63 0.11	23.15 0.04
2448679.0409.....	24.03 0.08	22.89 0.04	24.40 0.21	23.96 0.09	23.83 0.06	24.93 0.15	23.20 0.05
2448679.175*.....	...	...	22.76 0.06	22.42 0.05	23.01 0.07	...	21.96 0.05
2448684.2376.....	23.56 0.08	22.81 0.04	23.90 0.07	23.60 0.09	24.26 0.11	24.42 0.14	23.49 0.06
2448691.1064.....	24.13 0.14	22.93 0.04	23.21 0.04	23.45 0.06	23.48 0.05	24.60 0.11	23.56 0.06
2448694.7231.....	23.67 0.06	22.76 0.04	...	23.77 0.08	23.78 0.06	...	23.65 0.06

NOTE.—HJD values ending with (*) indicate F785LP observation and magnitudes.

Basel photometry, and is included both in Table 2 and Figure 2. The photometry procedure used at STScI rejected the object since it is too close to the edge of the frame, but it is clear from visual inspection that it is a bona fide variable—the photometry given in Table 2 for this particular object is from the Basel photometry.

Light curves could be obtained for 33 of the 39 variables above in the period range 2 to 45 days. The remaining six objects are either aperiodic or have periods in excess of 45 days that cannot be determined from the present observations covering a 47 day range. Alias problems are essentially nonexistent since the data sample the above period range extremely well, and there is no ambiguity about the periods. From the light curves, 29 objects are seen to be possible Cepheids. The light curves for these 29 are plotted in order of derived period in Figure 4. The remaining four variables for which we have light curves (last four panels of Fig. 4) are definitely not Cepheids.

For all the variables for which we have periods, we calculate the mean intensity and phase-weighted apparent magnitude in F555W:

$$\langle \mathrm{F555W} \rangle = -2.5 \log_{10} \sum_{i=1}^{n} 0.5(\phi_{i+1} - \phi_{i-1}) 10^{-0.4 m_i}, \quad (4)$$

where n is the number of observations, ϕ_i is the phase of the ith observation in order of increasing phase (after folding the period). Note that the above equation requires the nonexistent entities ϕ_0 and ϕ_{n+1}: ϕ_{n+1} is set identical to ϕ_1, and ϕ_0 is set identical to ϕ_n, which is just tantamount to allowing cyclical continuity across $\phi = 0$ (or $\phi = 1$). The phase-weighted method of estimating mean magnitudes is superior to a straight mean and, as discussed in Saha & Hoessel (1990), minimizes the systematic biases (from loss of faint measurements) in the mean magnitude.

Table 3 contains the summary information of all the variables. The derived periods are given in the second column, and

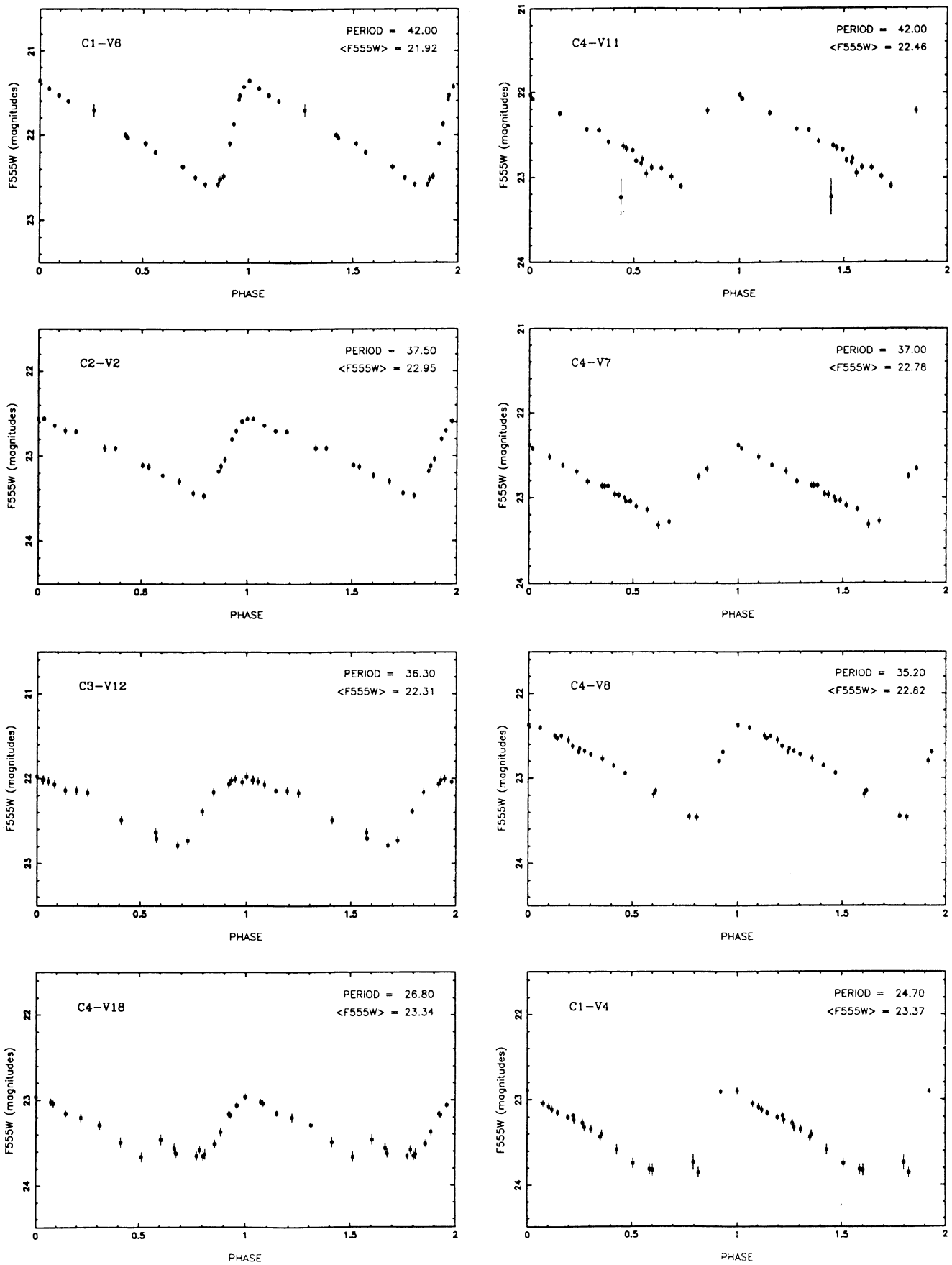

FIG. 4.—Light curves, mean magnitudes, and periods for variable stars discovered

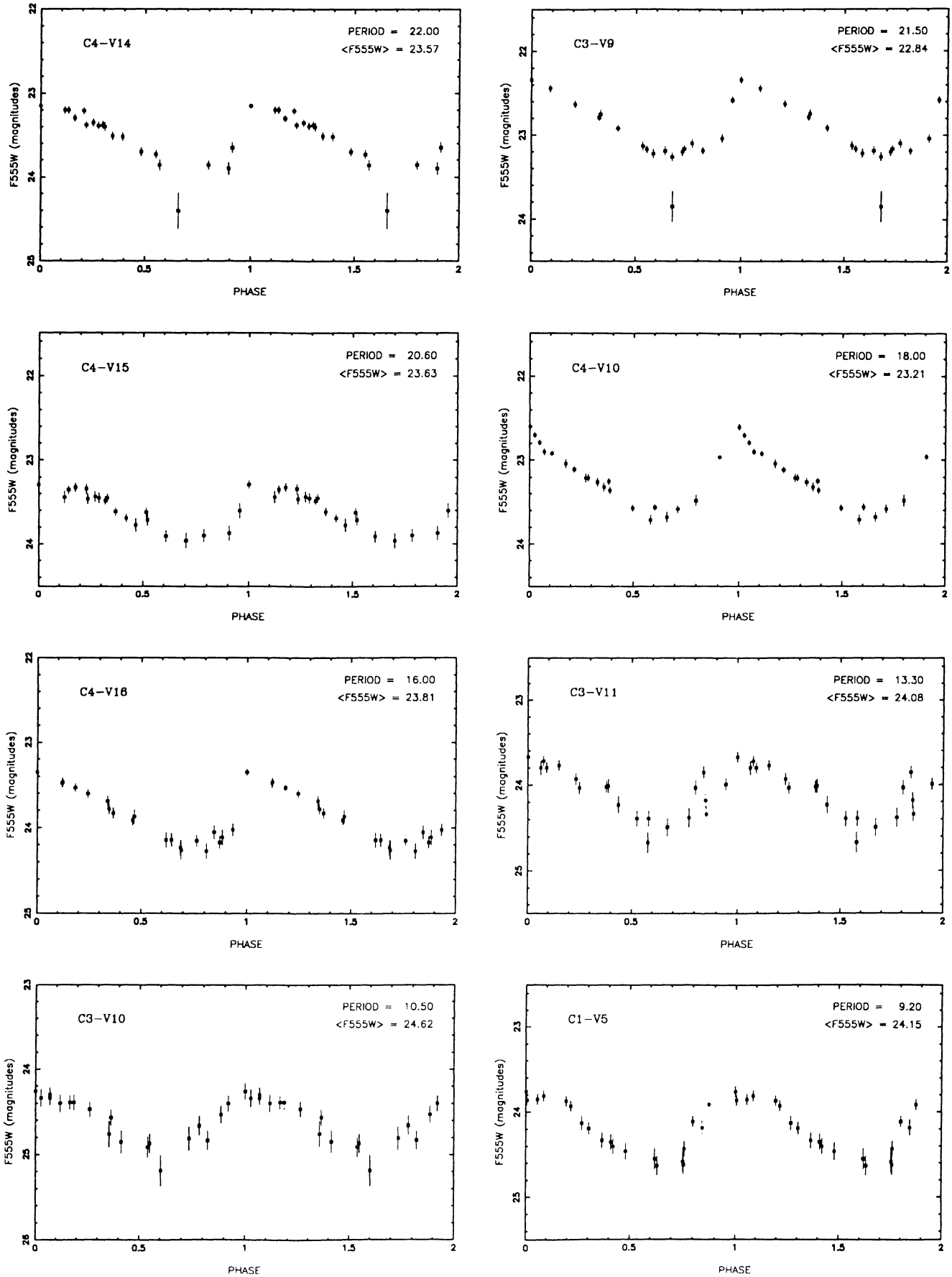

FIG. 4—*Continued*

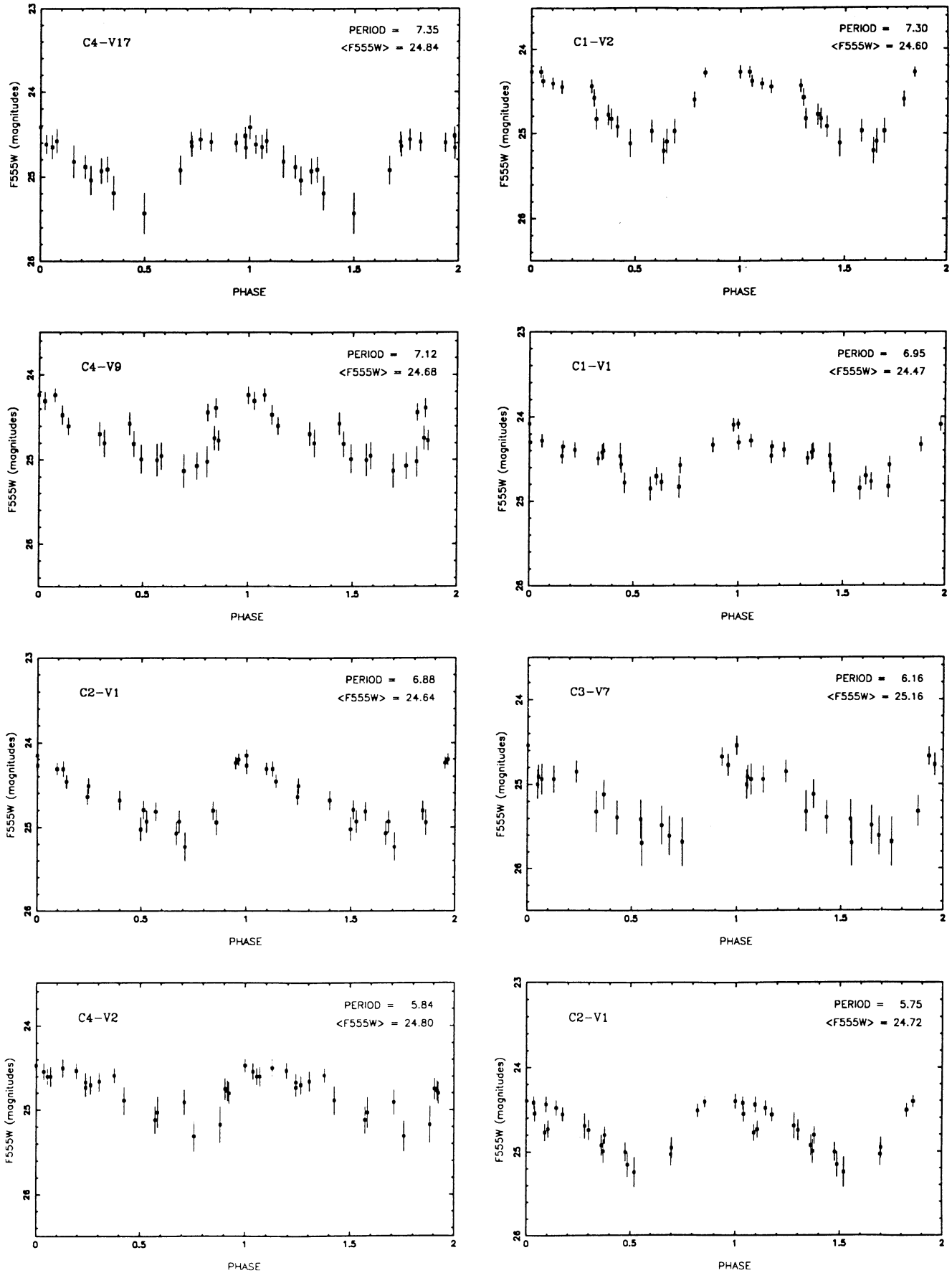

FIG. 4—*Continued*

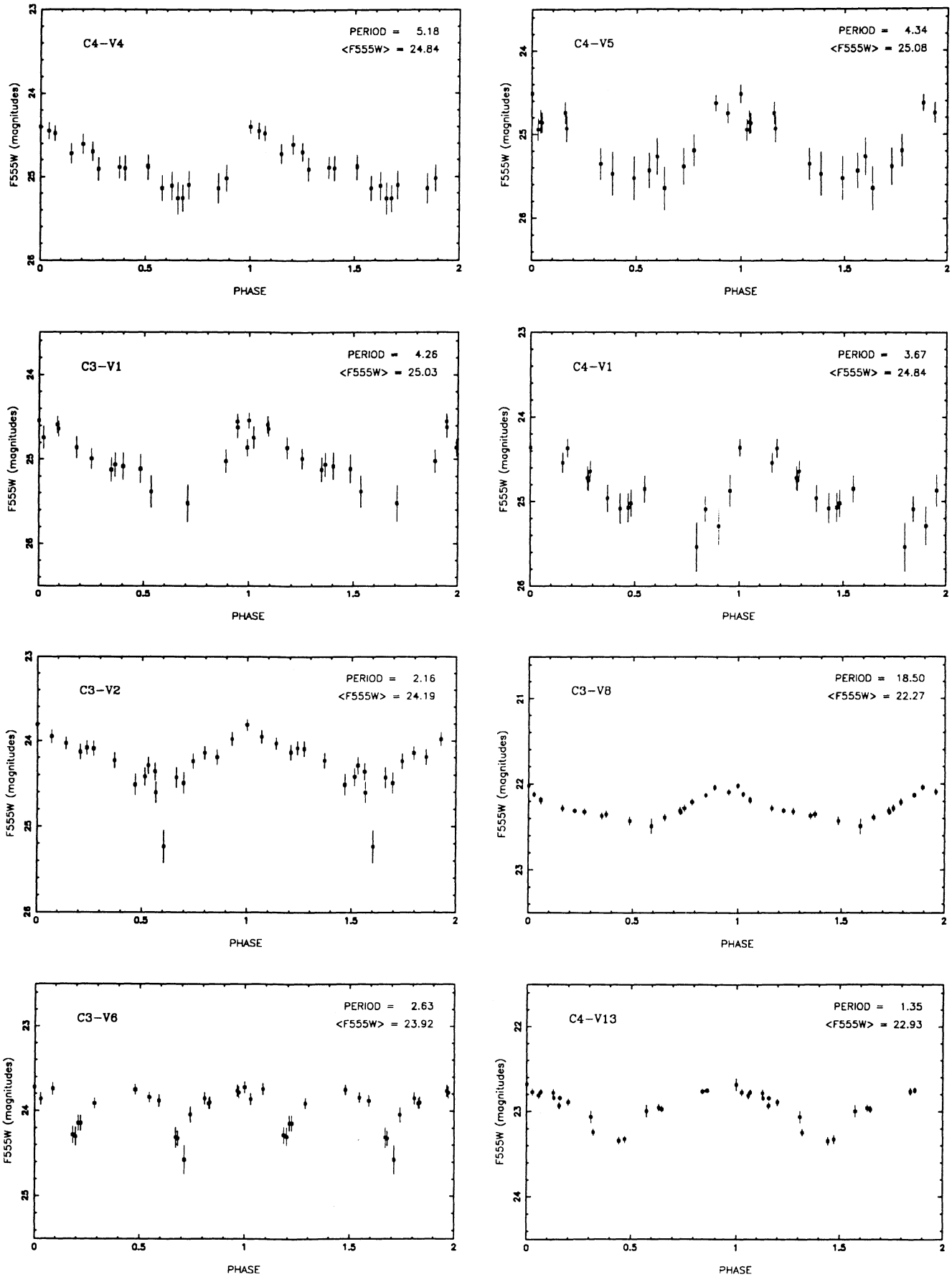

FIG. 4—*Continued*

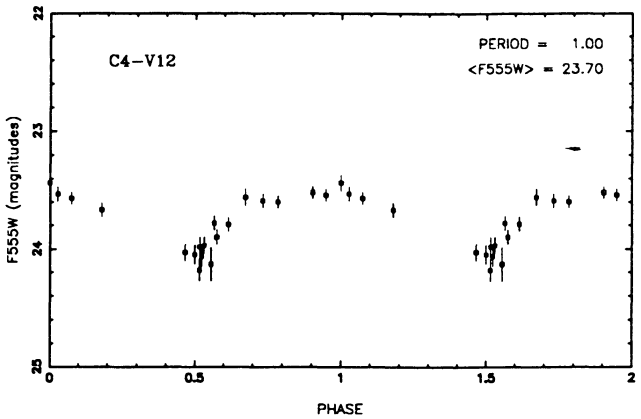

FIG. 4—*Continued*

the mean F555W magnitudes (calculated as above) in the third column. For the variables with unknown periods, a less certain mean magnitude is quoted, and individual measurements are available in Table 2.

4. PHOTOMETRY AND DETECTION OF VARIABLE STARS AT BASEL

This section describes the procedure followed in Basel, where the photometry was obtained independently from STScI and by utilizing different methodology than the one reported in the previous section. A first account is given in Labhardt, Schwengeler, & Tammann (1993). The reduction and analysis performed at the Basel Astronomical Institute used the ESO image processing system MIDAS (version NOV91). The reduction began with the data as initially processed by the calibration pipeline program at STScI (see Table 1).

4.1. *Preparation of the Original Date Sets*

The detection and removal of unwanted signals caused by cosmic rays and hot spots could not be solved to complete satisfaction. As a matter of fact, most cosmic rays can easily be recognized by both their sharply defined shape and their small width of either one or two pixels. Ideally, one simply had to compare—for each pair of exposures taken at the same epoch—the data values of all corresponding pixels and watch

TABLE 3

CHARACTERISTICS OF THE VARIABLE STARS

Object	Period (days)	⟨F555W⟩ (STScI)	⟨F555W⟩ (Basel)	⟨V⟩ (mean)	⟨F785LP⟩ (Basel)	⟨I⟩ (Basel)	Type	Remarks
C1–V1	6.95	24.47	24.56	24.47	23.65	23.71	Cepheid	
C1–V2	7.30	24.60	24.58	24.54	23.68	23.75	Cepheid	
C1–V3	...	24.4:	...	...	...	...	No period	
C1–V4	24.7	23.37	23.30	23.29	22.38	22.45	Cepheid	
C1–V5	9.20	24.15	24.11	24.10	23.51	23.55	Cepheid	
C1–V6	42.0	21.92	21.90	21.87	21.14	21.19	Cepheid	
C2–V1	5.75	24.72	24.65	24.65	23.80	23.86	Cepheid	
C2–V2	37.5	22.95	22.86	22.86	21.76	21.85	Cepheid	
C2–V3	6.88	24.64	24.58	24.57	23.96	24.00	Cepheid	
C3–V1	4.26	25.03	24.98	24.98	24.56	24.59	Cepheid	
C3–V2	2.16	24.19	...	24.2:	...	...	?	
C3–V3	...	24.6:	...	24.6:	...	...	No period	
C3–V4	...	22.4:	...	22.4:	...	...	Cepheid?	$P \geq 50$ days
C3–V5	...	25.3:	...	25.3:	...	...	?	
C3–V6	2.63	23.92	...	23.9:	...	...	Eclipsing	
C3–V7	6.16	25.16	25.30[a]	25.13	24.59	24.63	Cepheid	
C3–V8	18.5	22.27	...	22.2:	...	...	Cepheid?	Superposed stars?
C3–V9	21.5	22.84	22.78	22.80	22.59	22.60	Cepheid	
C3–V10	10.5	24.62	24.60	24.56	23.69	23.76	Cepheid	
C3–V11	13.3	24.08	24.07	24.04	23.22	23.28	Cepheid	
C3–V12	36.3	...	22.41	22.36	21.50	21.57	Cepheid	
C4–V1	3.67	24.84	25.23[a]	24.83	24.73	24.74	Cepheid	
C4–V2	5.84	24.80	24.84	24.80	24.40	24.43	Cepheid	
C4–V3	...	21.2:	...	24.2:	...	...	Red Variable?	
C4–V4	5.18	24.84	24.89	24.85	24.49	24.51	Cepheid	
C4–V5	4.35	25.08	25.46[a]	25.1:	...	...	Cepheid	F785LP too faint
C4–V6	...	20.4:	...	...	...	...	LBV?	
C4–V7	37.0	22.78	22.71	22.70	21.71	21.79	Cepheid	
C4–V8	35.2	22.82	22.67	22.72	22.13	22.17	Cepheid	
C4–V9	7.12	24.68	24.65	24.65	24.27	24.29	Cepheid	
C4–V10	18.0	23.21	23.10	23.14	22.75	22.77	Cepheid	
C4–V11	42.0	22.46	22.30	22.33	21.32	21.40	Cepheid	
C4–V12	1.00	23.70	...	23.7:	...	...	Eclipsing?	
C4–V13	1.35	22.93	...	22.9:	...	...	Eclipsing?	
C4–V14	22.0	23.48	23.46	23.42	22.55	22.62	Cepheid	
C4–V15	20.6	23.63	23.41	23.36	22.21	22.31	Cepheid	
C4–V16	16.0	23.81	23.78	23.76	23.06	23.11	Cepheid	
C4–V17	7.35	24.84	24.92	24.85	24.30	24.34	Cepheid	
C4–V18	26.8	23.34	23.15	23.20	22.17	22.25	Cepheid	

NOTE.—Objects with blank entries under the "Period" column are those for which there is definite variability, but no periodicity can be determined from the data to hand. Values ending with ":" are approximate due to missing information.

[a] Basel magnitudes poorly defined due to very low S/N. They were not used for the calculation of ⟨*V*⟩ (mean).

for obvious discrepancies. The prerequisites for such an anticoincidence check are (i) perfect registration on the CCD chip and (ii) the absence of any shift between successively recorded images.

With regard to (i), a comprehensive list of permanent defects (blocked columns and traps) is given by Lauer (1992). In the present work, only the corrupted columns and a few of the traps were modified on every image by approximation with a least-squares, second-order polynomial using the adjacent "good" pixels. The exposures W0UA0501T and ...I04T are affected by streaks from a moving object.

Condition (ii) was almost ideally met due to the superb pointing capability of *HST*. The spatial shift between two exposures taken at the same epoch amounted typically to 0.1 pixel, in a few cases up to a few tenth of a pixel. The shifts from one epoch to any other epoch ranges from 0 to 2 pixels; the maximum offset was 4 pixels. Nevertheless, this small shift due to nonperfect pointing of the telescope is extremely important in view of the severe undersampling of the WFC. The careless application of any cleaning procedure is likely to behead the brighter of the two intensity peaks registered for one and the same star at the same epoch.

As a result of many experiments it was decided to remove only signals detected above a fixed threshold, i.e., concentrate on the high- and medium-energy cosmic rays and leave the low-level cosmic rays which cannot be distinguished from faint stars. The average sky background level in star free regions is 21 DN with a rms scatter of 2.1 DN. The activation threshold was set to approximately 7 σ noise fluctuation (15 DN). The following procedure was applied to every back-to-back image pair with the exception of the incomplete case W0UA0J... and yielded the detection and replacement of some 4000 pixels affected by CR and hot-spots on every 800 × 800 frame.

1. On a pixel-by-pixel basis, a "clean" image is generated which takes the lower of the two parent values.
2. Each of the two parent exposures is separately compared with the clean image and all residuals are collected in the form of two difference images.
3. On any of the difference images, only those pixels are considered that are above the activation threshold. They get replaced by the value of the corresponding pixel in the other parent image.

Following the basic procedures established for the reduction and analysis of ground-based data (Labhardt, Spaenhauer, & Schwengeler 1991, 1992), the cleaned image pairs were coadded after alignment to within a fraction of a pixel (translation, rotation, and rebinning) to form one combined image for every epoch. The photometric consequence of this staking method (causing a slight broadening of the PSF) compared with the direct image addition after correction for linear shifts (keeping the original PSF) is addressed again in § 4.2. Initial experiments with image restoration based on ideas given in recent issues of the ECF Newsletter were soon abandoned because the mandatory flux conservation got violated and there was unavoidable increase of noise.

4.2. *Stellar Photometry*

As there was no tool available to perform optimum crowded-field photometry in the aberrated *HST* images, one again had to rely on previously gained experience and utilize procedures developed for the measurement of ground-based data. The ROMAFOT (Buonanno et al. 1979, 1983) package as implemented in the MIDAS environment was mainly used for this project. It fits a sum of elementary, analytically determined PSFs to the data set, simultaneously with an analytical plane for the description of the sky background. The program does not support the variation of the PSF across the field—a severe restriction when one is faced with a spatially and temporally changing PSF. The methodology to arrive at reliable instrumental photometry included the following steps.

1. *Construction of the PSF.*—As no reconstruction of the ideal PSF was attempted, and yet all the S/N was contained in the core of the severely undersampled WFC PSF, a simple fit of the central intensity peak was undertaken. Due to extreme crowding in WF3 and WF4 it was impossible to define the PSF from a sufficient number of stars for each of the four chips separately. Using all bright and isolated stars that could be found in WF1 to WF4, a "best" mean PSF was determined for F555W and F785LP and kept stable for all epochs. The values adopted for the fixed parameters of the uniform Moffat function (Moffat 1969) were $\beta = 4.0$, $\sigma_{F555W} = 2.20$ pixels, and $\sigma_{F785LP} = 2.40$ pixels.

2. *Selection and photometry of program stars.*—In order to get a most reliable search list as input for the fit procedure, five images were digitally added. Several attempts were undertaken to automatically detect all objects above the sky. However, this task becomes exceedingly difficult in crowded regions and in the vicinity of (bright) stars. The latter is covered with spikes and tendrils due to the aberration problem of the telescope. In addition, a substantial part of the spurious detections were created by low-level cosmic rays. The resulting lists contained up to several 10^4 mostly useless identifications per chip. These could in principle be excluded from further consideration after fitting the PSF with floating parameters. The size of σ is a good discriminator between stars and extended objects as well as almost pointlike CR hits. As a reasonable alternative to this impractical approach, and interactive star identification was done. For each of the four WFC fields a small but manageable object list with less than 200 hand-selected entries was compiled. This clearly subjective procedure resulted in unequal values for the limiting magnitudes of the four subfields. The actual fit was based on this unique set of input lists. It allowed for a varying but not tilted sky background. Every single measurement was evaluated by inspecting the displayed intensity profile and the superposed fit as well as the residual subimage. Through direct interaction, the fit quality was improved where necessary by adding stellar components, defining holes for the suppression of unwanted features like cosmic rays, and adjusting the dimensions and the shape of the windows in which to perform the fit. This time-consuming process resulted in four files holding a total of 600 instrumental stellar magnitudes for each of the 20 epochs.

3. *Correcting the photometry for temporal variations.*—At this stage the instrumental photometry was far from being homogeneous. The individual measurements were still affected by spatial variations of the PSF across the detector, differences of the PSF from chip to chip, and temporal variations. The latter were caused by changes of the PSF due to telescope jitter during the exposure, focus adjustments, and a series of decontamination events that changed the characteristics of the flat field over the whole time span of observations. The obvious impact on photometry of these various effects was not closely monitored by any external observing or calibration program. Our science data were not suited to correct for all the effects. Fortunately, there was a way to correct at least relatively for

the effect of temporal changes. Plotting the instrumental magnitudes of individual stars versus time (i.e., epoch) revealed a general pattern of fluctuation, the amplitude of which was much larger than our internal photometric errors. For every F555W image and epoch the average instrumental magnitude offset relative to the epoch with the highest count rate (thus the most sensitive state of the instrument) was determined, based on a sample of bright, intrinsically nonvariable stars. The latter were also selected to represent for each chip as fairly as possible the area actually covered by program stars. In this way there was partial removal of the spatial variation of the photometric zero point. The resulting magnitude corrections ranged from 0 to 0.2 mag (Fig. 5). All instrumental magnitudes were corrected accordingly and thereby put on a homogeneous photometric level. The two F785LP images were treated similarly; the first epoch served as photometric reference. The flat-field procedure puts the *full-aperture* magnitudes from the different chips on par. However since a PSF represents a fraction of the light, and since the individual reimaging cameras for the various chips can produce slight differences in the PSFs, our homogenized instrumental photometry is possibley still affected by intrinsic chip-to-chip variations. Thus the zero point corrections must be performed individually for each chip.

4. *Photometric zero-point correction.*—To get from the instrumental magnitudes to the standard magnitude system, which is the ground-based WFPC system described in Harris et al. (1991), we strongly relied on the information given by the SV Report. As a matter of fact, the basic zero-point constant depends on the camera, filter, flat field, contamination, the digital aperture used for the photometry, etc. In the SV Report, one can find the aperture corrections of the flight magnitudes for radii 5 to 35 pixels (Table 12.7) and the mean zeropoints relative to the ground-based WFPC system for full aperture (40 pixels) photometry (Table 12.15). Note that for each passband and all four WF cameras the SV Report gives only one value for the uniform photometric zeropoint, which is adequate since differences in sensitivity between the four CCD chips are accounted for in the pipeline flat-fielding procedure (see previous section). Before applying any of the published aperture corrections, the actual fraction of detected light covered by the ROMAFOT-returned PSF had to be determined. Due to either the severe crowding (WF1, WF3, WF4) or the lack of foreground stars in the region surrounding the target (WF1, WF2) the images contained not a single isolated star that is perfect for full aperture photometry. Therefore, growth curves were constructed from magnitude measurements taken with aperture radii of n pixels (where $n = 2, 3, 4, \ldots$). The sky brightness was estimated in a concentric annulus with radii of 40 and 50 pixels. On images from all four WF cameras, (F555W) and seven (F785LP) bright, isolated stars could be measured out to radii of 20 pixels without running into neighboring objects. Assuming that these growth curves would follow for all four WFC, the same filter specific template defined by the brightest star on WF2 (the correction from 20 pixel to 40 pixel apertures are not expected to be affected by differences in the individual reimaging cameras, but by the spherical-aberration problem that affects all chips in essentially the same way), every individual curve was shifted vertically to coincide with the template over the range from 12 to 20 pixel radius. The difference in brightness between the two curves was read at a radius of 20 pixels and used to correct the less well-defined curve for the effects of remaining CR spikes, variation of the sky background, and low S/N. The individual aperture corrections were weighted according to the curve's quality and averaged to $\Delta m_{\mathrm{PSF}\rightarrow r=20\ \mathrm{pix}} = 1.537 \pm 0.008$ mag for the F555W images and 1.764 ± 0.003 mag for F785LP.

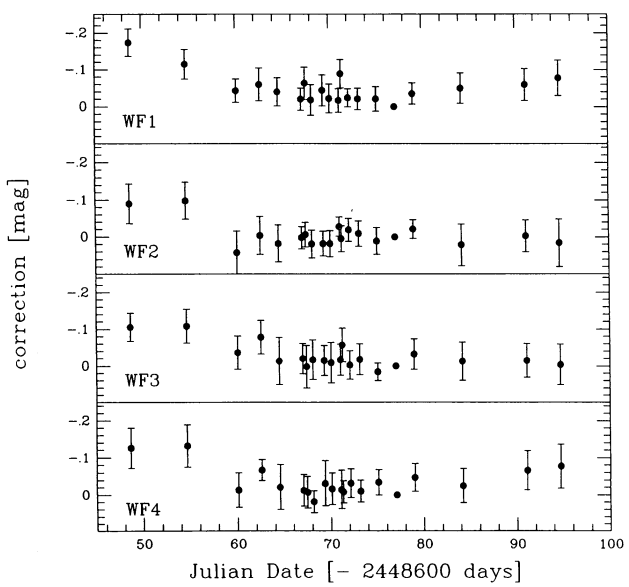

FIG. 5.—ROMAFOT magnitude corrections for each of the four chips relative to the epoch of maximum sensitivity, HJD 2448677. Each point is defined by the average of 13 to 25 stars.

The arithmetic combination of the above mentioned aperture corrections with the scaling to an exposure time of 1 s and the nominal zero-point constant finally resulted in the adopted additive correction of 30.398 mag (F555W) and 28.723 mag (F785LP) for translating the homogenized instrumental ROMAFOT magnitudes to the *HST* standard system. The internal accuracy of these constants is approximately ± 0.02 mag; the estimated error of the calibrated single measurements is 5 times larger. Note that the contamination problem introduced an additional photometric zero-point error of unknown size between our reference epochs (1992 February 24 for F555W, 1992 February 26 for F785LP) and the epoch at which the zero-point constants published in the SV Report were determined (1992 January 1). The internal accuracy of the homogenized data can be illustrated by the dependence of the statistical error of the F555W magnitudes, averaged over 19 epochs, on the mean magnitude (see Fig. 6 below). The limit of the latter is at ≈ 24.6 mag for the WF1 images, 23.4 mag for WF2, 23.8 mag for WF3, and 24.0 mag for WF4. The photometric measurements described above were made on images prepared by the stacking method (see § 4.1). A comparison with the photometry obtained from directly added back-to-back exposures revealed no systematic differences: owing to the narrower PSF, the growth curve analysis resulted in a somewhat larger (typically $+0.02$ mag) aperture correction to be applied.

As an external check of the photometric calibration, the V image taken from the ground by Kristian and Carlson (§ 3.2) was also measured with ROMAFOT in Basel. A total of 53 stars not too obviously affected by blends were used to compare the ground-based instrumental V magnitudes with the mean F555W magnitudes averaged over 10 epochs. The resulting zeropoint value was different for each of the four chips but always within ± 0.2 mag of the above mentioned

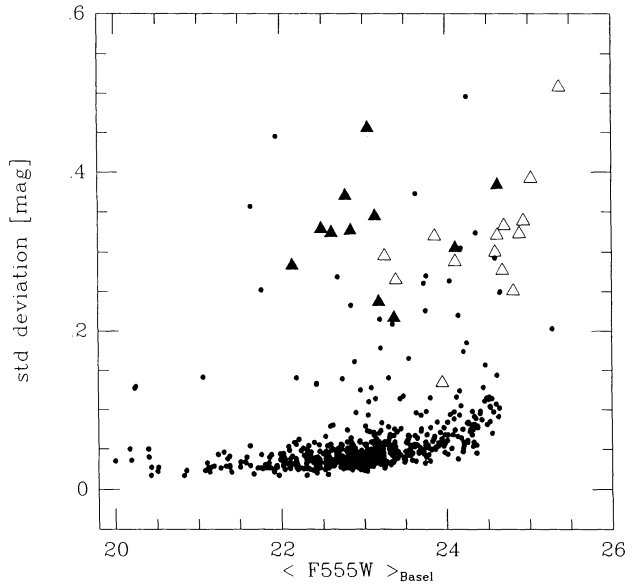

FIG. 6.—Statistical error of the F555W magnitudes, averaged for 19 epochs, is plotted as a function of the mean magnitude. Shown are the stars (*circles*) and Cepheids (*filled triangles*) found in Basel on images from all four chips, along with the subsequently measured Cepheids (*open triangles*) found in Baltimore.

constant. Differences between the two photometric systems (Harris et al. 1991) are negligible at this level of discrepancy. Clearly the data cannot improve the calibration provided by the SV Report. This is in part due to the ground-based quality of the frames. However, the error itself reflects the overall accuracy of our *HST* data. This statement is in good agreement with the corresponding findings at STScI (§ 3.3).

4.3. *Finding Variables and Determining Light Curves*

For all epochs, a matching procedure combined the valid F555W magnitudes belonging to the same object. The generated large data pool was searched for significant (>0.2 mag) brightness variations of its entries within the time span covered by the observations. The standard deviation of ⟨F555W⟩ provided a most efficient tool to single out variable stars. Its dependence on the mean instrumental magnitude is shown in Figure 6. There is a pronounced separation of variable stars from stable stars. Every suspect candidate star was first checked on all images for genuine variability by using the DAOPHOT I software (Stetson 1987) within MIDAS. The findings of ROMAFOT were fully validated. Then the light curve of each confirmed variable was generated and examined for its characteristics. Running a simple period finding program revealed 12 Cepheids and a couple of variables of different type.

Only at this stage did a detailed comparison take place of the photometry and list of bona fide candidates established independently at the two reduction sites (see also following section). With the exception of just one bright Cepheid (C3-V12) there was total agreement on the detected candidates found in the common part of the object search list. The procedure for determining the light curve and performing a periodicity test as described in § 3.4 was subsequently also used in Basel. Positions of the fainter candidates found at STScI on the basis of the much deeper DoPHOT photometry were used at Basel to get the corresponding ROMAFOT magnitudes for all F555W and the two F785LP images. However, no additional effort was undertaken to remeasure and reevaluate the full original object list created at STScI. The Basel ⟨F555W⟩ magnitudes are intensity means over the light curve, expressed in magnitudes, and shown in the fourth column of Table 3. The very low S/N of the three faintest Cepheids prevented ROMAFOT from returning reliable measurements. Therefore $\langle F555W\rangle_{Basel}$ below 25 mag were not considered for the determination of the final ⟨F555W⟩. Object C3-V12 was not treated by the procedure at STScI where it was deemed too close to the field edge. Detailed photometry of the non-Cepheids is presented only from STScI.

The ⟨F785LP⟩ magnitudes in the sixth coluum of Table 3, measured only in Basel, reflect intensity means as well, although they are based on observations at only two epochs. This turned out to be sufficient for constructing with very good accuracy the *shape* of the entire infrared light curve of normal Cepheids, if the light curve in the visual is known (Labhardt & Sandage 1993). The amplitude ratio and the phase shift are only a function of period.

4.4. *Comparison with Results Obtained at STScI*

The F555W magnitudes obtained independently at Basel and STScI for all stars measured in common are in agreement to within the measuring errors discussed above. The residuals calculated for individual images show no irregular distribution caused by any scale error. They attest a very consistent determination of the zero points in the photometry. The systematic difference (Basel-STScI) amounts to only a few hundredths of a magnitude.

The near congruity of the two searches over the magnitude interval in common indicates that the sample is nearly complete for at least the brighter Cepheids. Some Cepheids may have been lost to both searches due to overcrowding, but this is not a dominant effect. This is shown by the fact that 14 Cepheids were found in the most crowded field of WF4, but only three on chip 2, which has the lowest surface brightness. Also, all objects which fall into the instability strip of the color-magnitude diagram (see following section for CMD) were investigated ex post facto for variability, and no additional variables were found in this way. It is believed that the 34 nonvariables seen in the instability strip are just stable objects that are apparently scattered into the instability strip by noise and photometry errors.

The periods given in Table 3 carry exceptionally large errors, because the entire observing interval lasted only 46 days. The longest Cepheid periods may therefore have errors of ≈ 1 day. The shorter periods are uncertain in the first decimal. These errors, however, are of no importance for the following discussion.

The random error of the infrared magnitudes in the sixth column of Table 3 can be estimated since each of the two F785LP magnitudes provides a value of ⟨F785LP⟩ following the procedure of Labhardt & Sandage (1993). Thus, one finds a mean error of the adopted mean of 0.15 mag. It follows from the above that the compounded mean error of the colors ⟨F555W⟩ − ⟨F785LP⟩ is 0.18 mag to increase to 0.25 mag for the faintest Cepheids. Judging from the good definition of the light curves shown in Figure 4, one estimates the mean errors of amplitudes to be ≈ 0.1 mag.

5. THE *P-L* RELATIONS IN *V* AND *I* AND THE DISTANCE MODULUS FOR IC 4182

The mean F555W magnitudes obtained independently at the two sites were averaged into ⟨F555W⟩. The mean F785LP

magnitudes obtained at Basel only by the procedure described above were used in conjunction with the ⟨F555W⟩ modifications of the transformations given by Harris et al. (1991). Based on our analysis of *BVI* data taken from Landolt (1973, 1983, 1992), we approximate $(V-I) \approx (B-V)$ over the range $0.0 < (B-V) < 1.6$. Under this assumption there is

$$V = \text{F555W} - 0.0679(\text{F555W} - \text{F785LP}) + 0.0198(\text{F555W} - \text{F785})^2 , \quad (5)$$

and

$$I = \text{F785LP} + 0.0485(\text{F555W} - \text{F785LP}) + 0.0268(\text{F555W} - \text{F785LP})^2 . \quad (6)$$

Thus, the resulting $\langle V \rangle$ and $\langle I \rangle$ values, presented in the fifth and seventh columns of Table 3, are in the Johnson-Cousins standard system.

Prior calibrations of the Cepheid *P-L* relation in *V* from Cepheids in the Local Group are

$$M_V = -2.83 \log P - 1.37 \quad \text{(Sandage and Tammann 1968)}, \quad (7)$$

$$M_V = -2.78 \log P - 1.35 \quad \text{(Feast and Walker 1987)}, \quad (8)$$

$$M_V = -2.76 \log P - 1.40 \quad \text{(Madore and Freedman 1991, sample 1)}, \quad (9)$$

$$M_V = -2.88 \log P - 1.24 \quad \text{(Madore and Freedman 1991, sample 2)}. \quad (10)$$

The equations (9) and (10) are based on different samples of LMC Cepheids, as discussed in Madore & Freedman (1991). The calibrations in *V* are mutually consistent to within 0.1 mag in the period interval 3 to 40 days. This agreement is impressive if one notes that equations (7) and (8) are calibrated with Galactic Cepheids, whereas equations (9) and (10) are based on an *adopted* apparent LMC modulus of 18.83 in *V*, corresponding to a true distance modulus of 18.50. Furthermore, the calibrating Galactic Cepheids have higher metallicity than those in the LMC. This corroborates the Freedman & Madore (1990) result, from a study of Cepheids in three fields of M31 with different metallicity, that the *P-L* relation in *V* and longer wavelengths is quite insensitive to metallicity.

The only calibrated *P-L* relations in $\langle I \rangle$ are from Madore & Freedman (1991). Again, from the two different LMC samples they found

$$M_I = -3.06 \log P - 1.81 \quad \text{(Madore \& Freedman 1991, sample 1)}, \quad (11)$$

$$M_I = -3.14 \log P - 1.70 \quad \text{(Madore \& Freedman 1991, sample 2)}. \quad (12)$$

The period-luminosity relation for the 28 Cepheids in $\langle V \rangle$ and $\langle I \rangle$ is illustrated in Figures 7*a* and 7*b*, respectively. In Figure 7*a* the continuous line is a forced fit with a slope of −2.83, corresponding to the Sandage & Tammann (1968) *P-L* relation, and is in excellent agreement with the data. The dashed lines drawn ±0.40 mag from it indicate the projection of the finite width of the instability strip and thus the expected intrinsic scatter envelope around the ridge line. The mean scatter about the ridge line of 0.27 mag (and thus hardly affected by the measuring errors of about 0.1 mag) is exactly the same as that found by Madore & Freedman (1991). The four faintest Cepheids lie somewhat above the ridge line, suggesting the possibility of selection bias, although their overluminosity is supported by their relatively blue $\langle V \rangle - \langle I \rangle$ color, as discussed later. In Figure 7*b*, the force fit is with a slope of −3.06 corresponding to the Madore & Freedman (1991) sample 1. Again the slope fits the data perfectly. The envelope lines are now at ±0.32 mag from the ridge line. The mean error in measurement for $\langle I \rangle$ is 0.18 mag, and the observed scatter about the ridge line is 0.26 mag, which yields a formal intrinsic scatter of 0.19 mag, again in agreement with the 0.18 to 0.21 mag scatter found by Madore & Freedman (1991) for the LMC Cepheids.

The conclusion from the above is that the *P-L* relations in $\langle V \rangle$ and $\langle I \rangle$ are perfectly consistent with external data and can be directly compared with the *P-L* calibrations shown

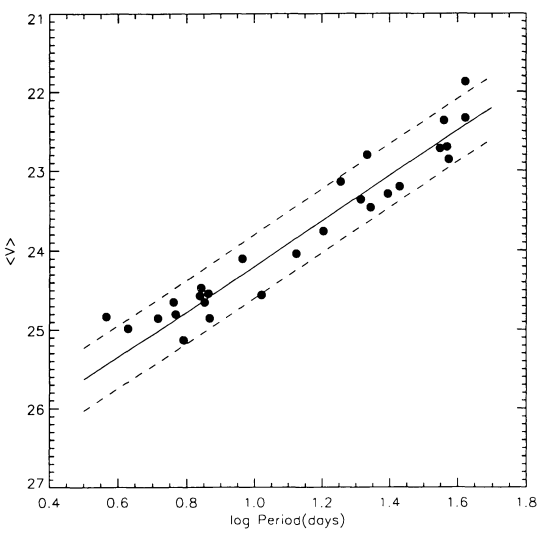

FIG. 7*a*

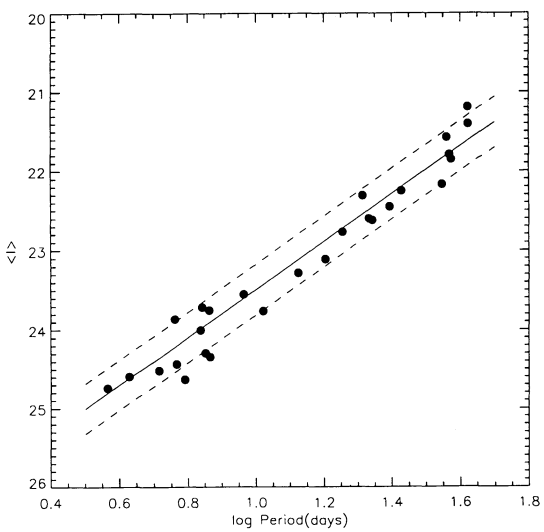

FIG. 7*b*

FIG. 7.—(*a*) *P-L* relation for Cepheids in IC 4182 in *V* (see § 5 for details). (*b*): *P-L* relation for Cepheids in IC 4182 in *I* (see § 5 for details).

TABLE 4

DISTANCE MODULI FROM CEPHEIDS IN IC 4182 FROM VARIOUS *P-L* RELATIONS

P-L Calibration	From $\langle V \rangle$ Data (28 Cepheids)	From $\langle I \rangle$ Data (27 Cepheids)
Sandage & Tammann 1968	28.36 ± 0.05, $\sigma = 0.26$	...
Feast & Walker 1987	28.29 ± 0.05, $\sigma = 0.27$	...
Madore & Freedman 1991, sample 1	28.31 ± 0.05, $\sigma = 0.27$	28.42 ± 0.05, $\sigma = 0.24$
Madore & Freedman 1991, sample 2	28.29 ± 0.05, $\sigma = 0.28$	28.40 ± 0.05, $\sigma = 0.24$
Mean	28.31 ± 0.05	28.41 ± 0.05
Overall mean	28.36 ± 0.05	

NOTE.—In addition, zero-point uncertainty in each of $\langle V \rangle$ and $\langle I \rangle$ is ≈ 0.1 mag.

above to derive the apparent distance to IC 4182. For the data and fits shown in Figures 7*a* and 7*b*, the difference of the observed intercept from the constant terms in the corresponding *P-L* relations cited above directly yields the apparent distance modulus. Similarly, the apparent moduli corresponding to the other *P-L* relation calibrations mentioned above can be derived. The results are summarized in Table 4. Additional allowance of 0.1 mag should be made to accommodate errors in the zero-point determination in each passband.

Comparing the results of $(m - M)_V$ and $(m - M)_I$ obtained from the Madore & Freedman (1991) *P-L* relations in *V* and *I* we find that $(m - M)_V - (m - M)_I = -0.11(\pm 0.15)$ (allowing for 0.1 mag zero-point errors in each passband) for each of their two samples. Since we are dealing with self-consistent *P-L* relations derived by them, we conclude that the formal value of E_{V-I} is therefore -0.11 ± 0.07. Using $A_V/A_I = 1.7$ (Scheffler 1982), we thus obtain formally

$$A_I = 1.43E_{V-I} = -0.16 \pm 0.21 , \quad (13)$$

$$A_V = 2.43E_{V-I} = -0.27 \pm 0.36 . \quad (14)$$

The extinction cannot be negative, and the above results are statistically consistent with zero extinction. A more rigorous statement is that extinction in both *I* and *V* is less than 0.1 mag. We thus adopt $A_I = A_V = 0.0$, which implies that the overall mean from Table 4 is the best estimate of the true distance modulus. The uncertainties quoted in Table 4 reflect the statistical errors and must be compounded with the zero-point error of 0.1 mag in each of *V* and *I*. This makes $(m - M)_V = 28.31 \pm 0.12$ and $(m - M)_I = 28.41 \pm 0.12$. The best estimate of the true distance modulus of IC 4182 is the overall mean:

$$(m - M)_{\text{true}} = 28.36 \pm 0.09 . \quad (15)$$

Any errors that result from adopting zero extinction are not included in the above uncertainties. A 3 σ lower limit of $(m - M) = 27.94$ can be placed from the value of $(m - M)_I$ and estimated value and uncertainty in A_I. Other estimates of extinction will be reported in the following sections.

The 14 Cepheids in chips 1, 2, and 3 yield $(m - M)_V = 28.34 \pm 0.08$, and the 14 in the crowded chip 4 field give $(m - M)_V = 28.38 \pm 0.06$, where the uncertainties are the statistical errors and do not include the zero-point uncertainties. The agreement in moduli to 0.04 mag demonstrates that

1. Magnitude zero points, which are evaluated independently in each chip, show very good consistency, which demonstrates that the evaluated zero points are essentially the same for the crowded and sparse areas of the field, and may in fact be much better than the conservative uncertainty estimate of 0.1 mag.

2. There is no evidence for different extinction as one goes from the crowded to sparser areas of the field.

6. PROPERTIES OF THE INSTABILITY STRIP

Consider the location of Cepheids on a color-magnitude diagram (CMD): the lines of constant period cross the CMD plane with negative slope. Hence they traverse the finite width of the nearly vertical instability strip at higher luminosities in the blue than in the red (see, for example, Sandage 1957, 1972; Sandage & Tammann 1968). Thus, a Cepheid that is relatively blue compared to one with the *same period* that is relatively red is expected to be more luminous. To first order, the magnitude residuals, R_V, of individual Cepheids with respect to the mean ridge line of the *P-L* relation are expected to correlate with the color. More generally, there should be a period-luminosity-color (*P-L-C*) relation that has no intrinsic scatter. The *P-L* relation is a projection of the *P-L-C* relation, as is the *P-C* relation, where each has intrinsic scatter since the third variable is disregarded. It is worth examining the *P-C* and *P-L-C* relations for the IC 4182 Cepheids and comparing them with other empirical data, as well as against theory.

6.1. *The Period-Color Relation*

The data from IC 4182 are plotted on the period-color plane in Figure 8. The formal regression of $\langle V \rangle - \langle I \rangle$ on log *P* yields

$$\langle V \rangle - \langle I \rangle = 0.43 \log P + 0.16 , \quad (16)$$

where the 1 σ uncertainty in the slope is ± 0.23, and where the

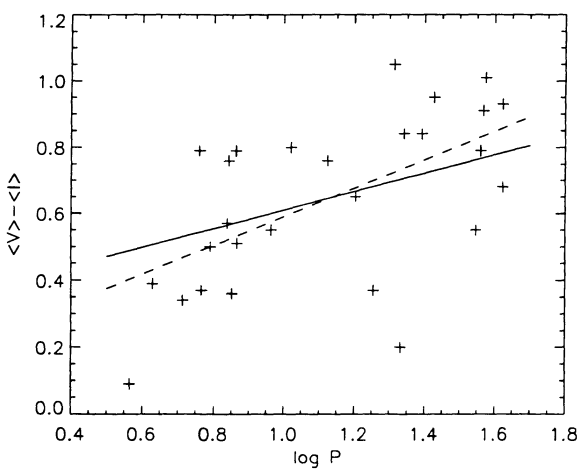

FIG. 8.—Period-color correlation for Cepheids in IC 4182 (see § 6.1 for details).

residuals in $\langle V\rangle - \langle I\rangle$ scatter by $\sigma_{V-I} = 0.21$ mag. This is shown in Figure 8 by the dashed line.

An empirical ridge line of the *P-C* relation can be found by subtracting equation (11) from (9), and also (12) from (10) for the two LMC samples studied by Madore & Freedman (1991):

$$\langle V\rangle - \langle I\rangle = 0.30 \log P + 0.41 , \quad (17)$$

$$\langle V\rangle - \langle I\rangle = 0.26 \log P + 0.46 . \quad (18)$$

A forced fit to the IC 4182 Cepheids with a slope of 0.28 (mean of the above equations) yields

$$\langle V\rangle - \langle I\rangle = 0.28 \log P + 0.33(\pm 0.04) \quad (19)$$

and leaves residuals with $\sigma_{V-I} = 0.21$ mag. This fit is shown in Figure 8 by the continuous line. Since this fit with the forced slope leaves residuals with identical σ_{V-I} as that by independently fitting the slope, the two solutions are statistically indistinguishable. This scatter is only marginally larger than the estimated color error of 0.18 mag, leaving a formal value for the intrinsic width of the *P-C* relation at 0.11 mag, which holds no surprises.

The intercept of the force-fitted *P-C* relation shows that $\langle V\rangle - \langle I\rangle$ is smaller than that from the Freedman and Madore LMC samples by ≈ 0.1 mag. This is simply a restatement of the result that the formal value of E_{V-I} is -0.11. The most obvious explanation is (small) zero-point photometric errors, as estimated in previous sections; it would be stretching the data to infer a difference in intrinsic colors of IC 4182 Cepheids compared to LMC Cepheids.

6.2. *The Period-Luminosity-Color Relation*

The *P-L-C* relation can be expressed to first order as

$$M_V = \alpha \log P + \beta(\langle V\rangle - \langle I\rangle) + C . \quad (20)$$

To fit such a relation to the IC 4182 Cepheid data at hand, the least well determined quantity $\langle V\rangle - \langle I\rangle$ is made the dependent variable, and a bilinear regression gives

$$\langle V\rangle - \langle I\rangle = 1.553 \log P + 0.413V - 10.95 , \quad (21)$$

where the 1 σ uncertainties in the coefficients of log P and V are quite large: 2.05 and 0.72, respectively. The scatter in $\langle V\rangle - \langle I\rangle$ is 0.176, again what is expected from our error estimates. Inclusion of higher order terms (involving $(\log P)^2$, V^2, or $V \log P$) does not reduce the scatter in $\langle V\rangle - \langle I\rangle$, and thus there is no justification for them. The slope of (and uncertainty in) the color term in the *P-L-C* relation follows trivially from the above, but the formal value of

$$\frac{\partial V}{\partial(\langle V\rangle - \langle I\rangle)} = 2.42 \quad (22)$$

is very poorly constrained by the data, essentially as a result of the large uncertainties in the measured magnitudes and colors. To properly solve for the *P-L-C* relation would require magnitudes and colors measured to accuracies of ≈ 0.03 mag.

7. THE COLOR-MAGNITUDE DIAGRAM

In order to get a meaningful color-magnitude diagram (CMD) based on consistent photometric measurements, the images of the two epochs with both F555W and F785LP exposures were reanalyzed. For this purpose, the tables containing positions and trial magnitudes for some 12,500 objects originally found by DoPHOT at STScI were passed to Basel. A Moffat profile with floating parameters was fitted by ROMAFOT to the images of only those objects that had been classified by DoPHOT as either "perfect" stars, components of a close pair, or faint objects where object classification is impossible. Convergent magnitudes resulted for ≈ 7000 and 3600 objects on F555W and F785LP images, respectively. After matching those objects that were successfully measured for both bandpasses and at each of the two epochs, there remained a total of 1100 starlike objects with $1.5 < \sigma_{PSF} < 4.0$ (typical value for a well defined star is 2.2).

Figure 9 shows the CMD without any identified Cepheid in the *HST* photometric system. The symbols distinguish between stellar objects, galaxies ($\sigma_{PSF} \geq 4.0$), and cosmic rays or defects ($\sigma_{PSF} \leq 1.5$). As expected, the latter mainly occupy the faint part in the diagram. The instability strip between the populations of the most luminous blue and red supergiants contains a relatively large number of stars. The predicted estimated number of field stars given by Ratnatunga & Bahcall (1985) allow for only five stars with $V < 25$ and $(B-V) < 1.3$ mag within the field of view of the WFC. An empirical check of the contamination by galactic stars was based on a set of F555W and F785LP images of the dwarf galaxy GR 8 extracted from the *HST* archive. This galaxy is located at almost the same galactic latitude as IC 4182 and is small enough to provide on the WFC large patches of "empty" sky. A complete analysis of its CMD and the contamination by foreground stars revealed similar results for the bright end, namely just six field stars above F555W = 24 mag. For the magnitude range $24 < V < 25$, some 90 stars or galaxies were found (extrapolated to the full image area).

Figure 10 shows the stellar content of IC 4182 (i.e., all objects plotted as filled circles in Fig. 9) after transformation to the Johnson-Cousins *VI* system. We recall that the relevant transformation equations (5) and (6) are strictly valid only for $0.0 < (V-I) < 1.6$. The instability strip falls right into this color range and accommodates all discovered Cepheids, plotted according to their mean *VI* photometry given in

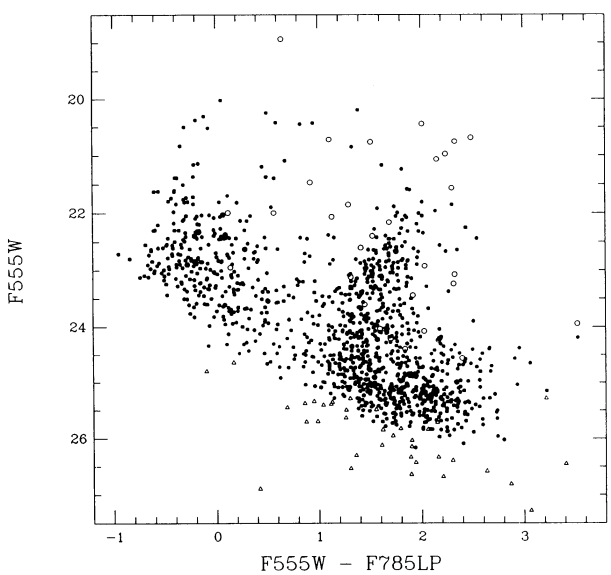

FIG. 9.—CMD of IC 4182 based on the combined photometry of epochs 3 and I. Stars (*filled circles*), galaxies (*open circles*), and cosmic rays or defects (*triangles*) were classified by DoPHOT. The ROMAFOT photometry is on the *HST* system. Cepheids are not shown in this graph.

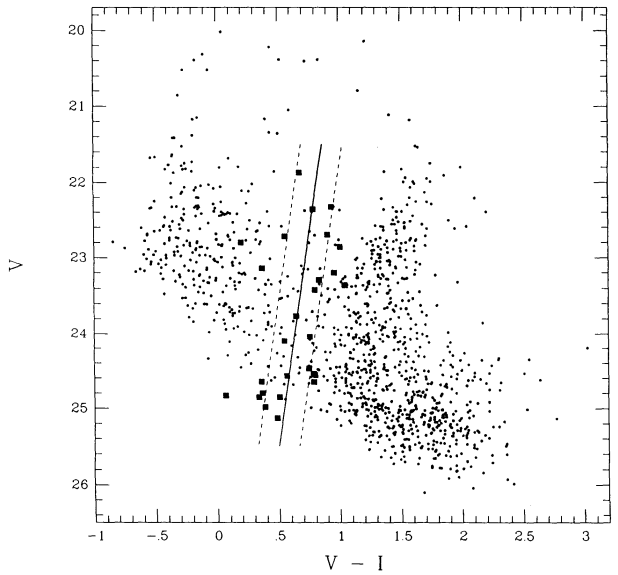

FIG. 10.—The stellar content of the CMD of Fig. 9 after transformation to the *VI* standard system. The 27 discovered Cepheids (*filled squares*) are included. The ridge line is from eqs. (10) and (12). The dashed envelope lines are drawn at ±0.17 (see text).

Table 3. The ridge line is defined by equations (10) and (12) and supplemented by envelope lines drawn at ±0.17 mag in $(V-I)$ (which corresponds to an intrinsic width in the *P-L* relation of ±0.50 mag in V, in conjunction with the derived empirical slope of lines of equal period in eq. [22]).

A detailed investigation of all 34 objects which fall into the instability strip of the CMD and were not already known as variables did not bring out any additional variables. One therefore has to assume that these stable objects in the instability strip are incorrectly placed in the CMD due to scatter of the magnitudes and colors and/or because they are not single stars.

8. RESOLUTION OF THE OLD GIANTS

An aggregate image of the field region in chip 4 was made by coregistering and co-adding 19 of the 20 individual epochs in F555W. Figure 11 (Plate 7) displays this composite image. The display parameters are set to show the low-level faint features and "burns" out the brighter areas. It is immediately apparent that the field is dotted with faint stars. The modified DoPHOT program was run on this very deep image, and it identified several thousand bona fide stars with F555W > 25.5 mag. A histogram of the magnitudes of unambiguous stars identified by the program on this image is shown in Figure 12.

The sudden (as one steps fainter) resolution into stars is exactly the effect noted by Baade (1944) for the bulge of M31, and the sheet of resolved stars are the brightest Population II giants, which are known to have maximum absolute V magnitude ≈ -2.5. Note from Figure 12 that the steep rise in numbers happens at F555W $\approx$ 26.0. For the present argument we take F555W magnitudes to be the same as V, and so derive a distance modulus to IC 4182 of $\approx$28.5. To within the expected uncertainty of this method, there is excellent agreement with the Cepheids.

Since IC 4182 is face on, any major internal extinction within it would lie along a thin sheet perpendicular to the line of sight, i.e., corresponding to the "disk." The older Population II stars can lie far from the disk. Thus, the brightest resolved giants must lie on our side of any alleged wall of extinction. Thus, the resolved brightest Population II giants must be essentially unaffected by internal reddening. The agreement of the distance moduli from this method and the Cepheids to within 0.2 mag is again a demonstration that internal extinction in IC 4182 is not an issue.

9. THE PEAK BRIGHTNESS OF SN 1937C

SN 1937C is the prototype of SNe Ia. It has exceptionally extensive and careful photometry in the m_{pg} system (Baade & Zwicky 1938) and in the m_{vis} system (Beyer 1939). The high internal accuracy of the photometry is demonstrated by the small scatter and by the fact that the light curves perfectly fit the template light curves of SNe Ia by Leibundgut et al. (1991) (this source contains also a compilation of some additional photometric data). It is possible to strengthen the zero point of the old photometry and to convert the data into the modern B, V system from subsequent photometry of the standard stars. The pg and vis maxima are discussed in turn.

9.1. *The Blue Maximum of SN 1937C*

The photometry of Baade & Zwicky (1938) begins just after maximum. With the template light curves for the pg magnitudes, it is therefore possible to determine a very reliable maximum magnitude in the internal pg system. The result is

$$m_{pg}(\max) = 8.50 \pm 0.05 \, . \qquad (23)$$

The photometric standard stars in the field used by Baade and Zwicky were remeasured by Mihalas (1963). He converted his measured B magnitudes into the m_{pg} system by means of Arp's (1961) transformation equation (case 3 of the various different definitions of m_{pg} is the one applicable here:

$$m_{pg} = B - 0.29 + 0.18(B-V) \, . \qquad (24)$$

Table 5 shows a comparison of Mihalas' final pg magnitudes against the original Baade and Zwicky values. In addition, UBV magnitudes of the local standard c (HD 113 730) were measured by Westerlund (1963); they are also used to obtain the pg magnitude using the above transformation.

The comparison is also shown graphically in Figure 13. The scatter of Baade and Zwicky's m_{pg} magnitudes is only 0.05 mag

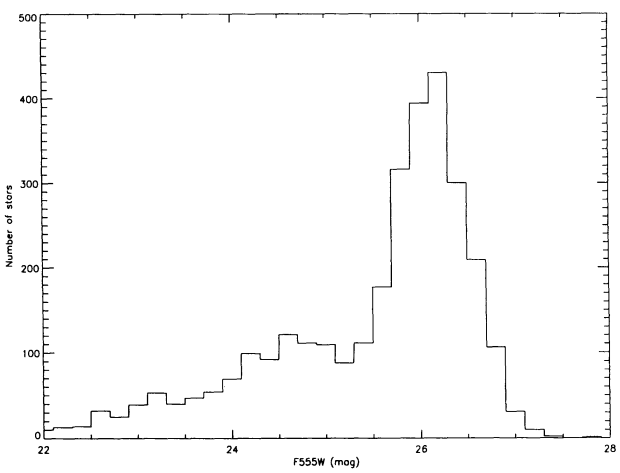

FIG. 12.—The histogram of ⟨F555W⟩ magnitudes for all starlike objects in the field of chip 4 detected on the aggregate image of 19 exposures.

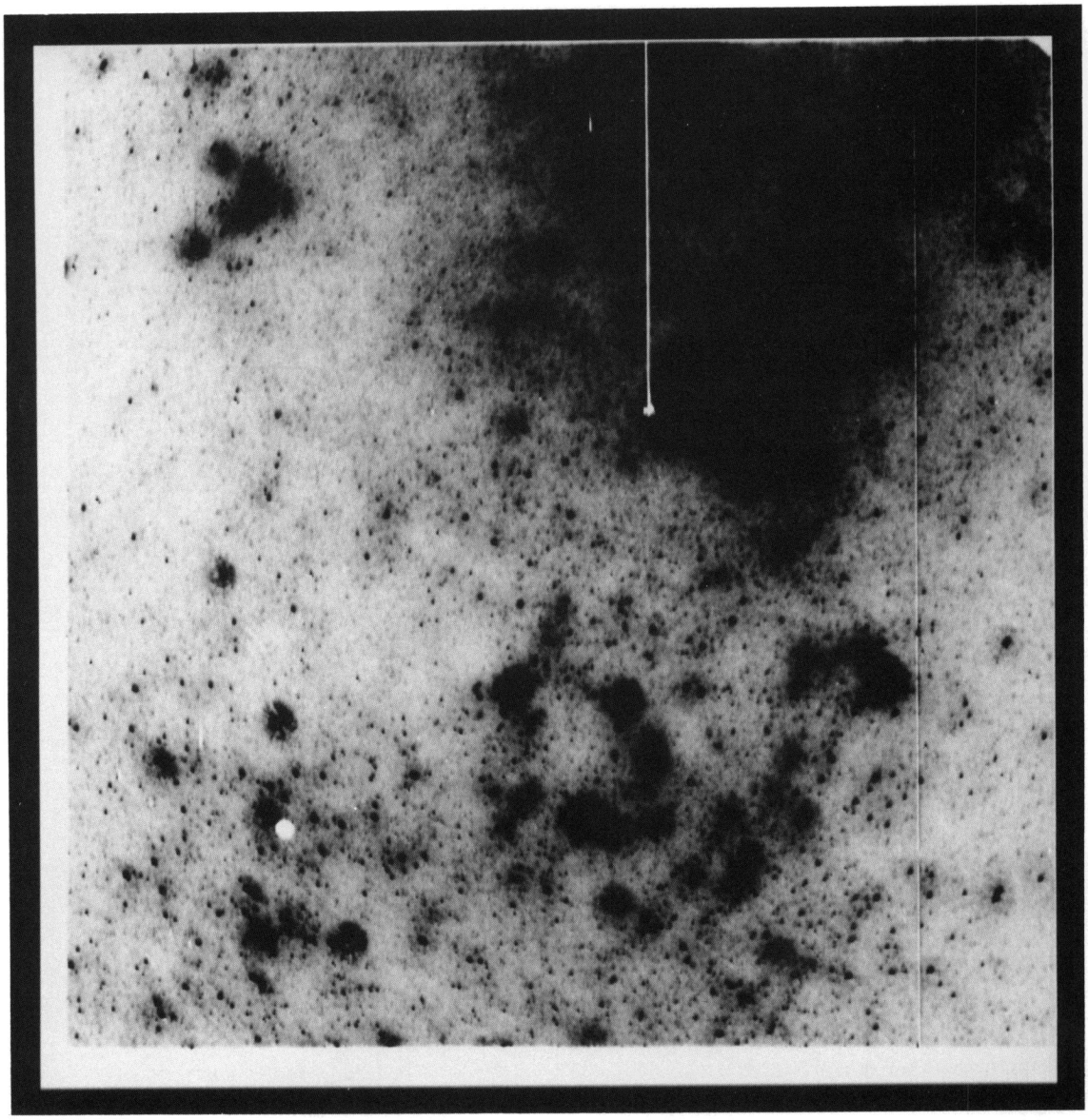

FIG. 11.—The aggregate image of 19 exposures for the Chip 4 field that shows resolution of the Population II giants

TABLE 5

BLUE PHOTOMETRIC STANDARDS FOR SN 1937C

Star Identification[a]	m_{pg}[a]	m_{pg}[b]
A	8.37	8.48
a	8.66	...
b	8.93	8.93
c	9.11	9.10[c]
d	9.74	9.66
e	9.79	9.78
f	10.03	9.89
g	10.79	10.76
h	10.85	10.70
i	10.78	10.69

[a] Baade & Zwicky 1938.
[b] Mihalas 1963.
[c] Taken from Westerlund 1963.

TABLE 6

VISUAL PHOTOMETRIC STANDARDS FOR SN 1937C

Star Identification	BD Catalog Identification	m_{vis}[a]	m_{vis}[b]	m_{vis}[c]
a	38 2403	8.10	...	...
b	37 2369	8.55	...	8.68
c	37 2367	8.78	8.68	8.69
d	39 2597	9.03	...	9.18
e	38 2398	9.05	9.21	...
f	38 2402	9.41	9.64	...
g	38 2400	9.68	...	9.82
h	38 2401	9.80	...	...
k	38 2405	9.84	10.09	...
m	38 2397	10.11	10.29	...

[a] Beyer 1939.
[b] Mihalas 1963.
[c] Others.

(!), but their stars with $9.75 < m_{pg} < 14.2$ are fainter, on average, by 0.07 mag. Yet the two or three standards which bracket the supernova at maximum are, if anything, too bright on the old scale. Reading from Figure 13, a correction of +0.07 mag is thus applied to the Baade and Zwicky value 8.50, and with this marginal correction, one obtains for SN 1937C,

$$m_{pg}(\max) = 8.57 \pm 0.10 . \quad (25)$$

The value of B_{max} is derived in § 9.3, after presenting the data for the visual maximum, so that the color terms can be evaluated.

9.2. *The Visual Maximum of SN 1937C*

The light curve of SN 1937C as collated by Leibundgut et al. (1991) gives

$$m_{vis}(\max) = 8.55 . \quad (26)$$

The available observations begin 10 days after B maximum. Since V maximum is known to follow the B maximum by 2.5 days (see Leibundgut et al. 1991), and since the observations follow the standard light curve of SNe Ia very well, the extrapolation to V maximum is well constrained. The observations were made by Beyer (1939), who was known as a very careful observer of variable stars, at Hamburg Observatory. He tied his local photometric comparison stars to the Harvard Revised Photometry sequence. Eight of his local standards have since been measured in the UBV system, five by Mihalas (1963), and three additional ones were provided by the Centre des Données Stellaires. The stars with their old and new photometry are listed in Table 6 and shown graphically in Figure 14.

On average, Beyer's magnitudes are brighter by 0.13 mag than the V magnitudes, with a scatter of only 0.1 mag. Beyer's comparison star c is given little weight, since it must be suspected to be variable: modern photometry gives very nearly equal brightness for the comparison stars b and c, whereas Beyer estimated c to be 0.23 mag fainter than comparison star b, and the discrepancy is considerably more than can be attributed to a photometric error by Beyer. As a compromise, a correction of 0.09 mag (faintward) to Beyer's magnitudes is adopted, and it follows that

$$V_{max} = 8.64 \pm 0.10 , \quad (27)$$

where the quoted uncertainty includes the error in fitting the template visual light curve and the conversion into the modern V system.

9.3. *The Color of SN 1937C*

To deduce the value of $m_B(\max)$ from the above data it is necessary to account for the fact that epoch of light maximum is different at different wavelengths. We adopt the time of maximum in B to be the epoch of maximum, unless otherwise qualified, so by $(B-V)_{max}$ we mean $B-V$ at epoch of B_{max}. Allowing for the fact that V_{max} occurs about 2.5 days after B_{max}, one obtains from the template light curves the simple relation

$$(B-V)_{B(\max)} = B_{max} - V_{max} - 0.02 \quad (28)$$

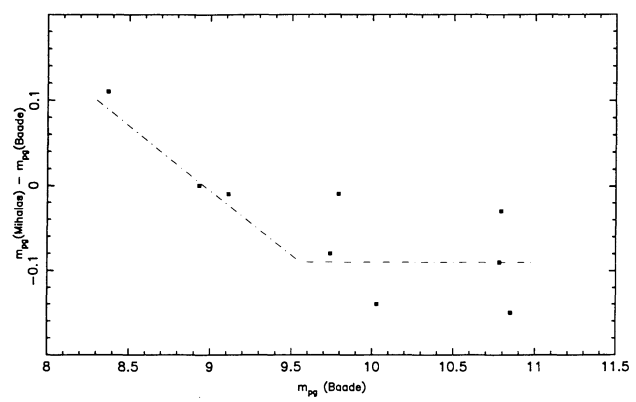

FIG. 13.—Comparison of Baade and Zwicky's *photographic* magnitude sequence to photoelectric measurements (see § 9.1).

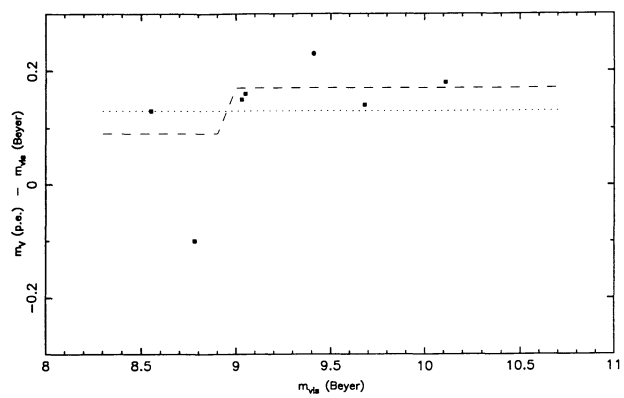

FIG. 14.—Comparison of Beyer's *visual* magnitude sequence to photoelectric V magnitudes (see § 9.2).

(Cadonau 1987; Sandage & Tammann 1993). It follows from equations (24), (25), (27), and (28) that

$$B_{\max} = 8.83 \pm 0.11 , \quad (29)$$

and

$$(B-V)_{B(\max)} = 0.19 \pm 0.15 . \quad (30)$$

The observed $(B-V)_{\max}$ values of the Sandage & Tammann (1993) sample of 34 SNe Ia values range from -0.32 to $+0.66$. This is almost certainly larger than the instrinsic dispersion in colors at maximum; the observed dispersion can be caused by some combination of three effects:

(1) intrinsic dispersion of colors at maxima of type Ia supernovae,

(2) reddening by dust in the host galaxy, and

(3) errors in the measured colors, particularly due to improper transformation of photometry to the standard Kron-Cousins system.

The relative importance ascribed to each of the above sources of color scatter can lead to vastly different conclusions. A detailed discussion given by Sandage & Tammann (1993) and the various scenarios are not repeated here. We note only with satisfaction that equation (30) agrees within the errors with their preferred mean color of SNe Ia of $(B-V)_{B(\max)} = 0.09 \pm 0.04$, but in any case, the approach taken in this paper circumvents having to rely on colors of SNe Ia as a class.

9.4. *Calibration of SN 1937C*

Using our best estimate of the distance modulus for IC 4182 (eq. 15), we obtain from equations (25), (27), and (29) the following values for the peak absolute magnitudes of SNe 1937C in the various passbands:

$$M_{pg}(\max) = -19.79 \pm 0.13 , \quad (31)$$

$$M_B(\max) = -19.51 \pm 0.14 , \quad (32)$$

$$M_V(\max) = -19.72 \pm 0.13 . \quad (33)$$

Note that the value of M_V derived above is essentially independent of the adopted extinction and only altered if there is a difference in the extinction to SN 1937C relative to the mean extinction to the Cepheids. The colors implied by the above equations are valid, provided the extinction to SN 1937C is negligible.

10. A PRELIMINARY VALUE FOR H_0

10.1. *The Hubble Diagram From SNe Ia*

Evidence that the absolute magnitudes at maximum of type Ia SNe have only a small dispersion has been reviewed by Branch & Tammann (1992). The basis is

(1) Uniformity of light curves,

(2) homogeneity of the spectra at various times at maximum and beyond,

(3) the near identity of the observed apparent magnitudes at maximum for SNe Ia in three galaxies, each of which have produced two such supernovae,

(4) same observed apparent magnitudes of the 10 SNe Ia observed in galaxies in the Virgo cluster, and

(5) the excellent agreement of the absolute magnitude calibration done by several independent means, including theoretical calculations.

It is acknowledged that there is a class of "peculiar" SNe Ia, which are underluminous, but these can be identified a priori from peculiarities in their light curves, spectra, and/or energy distribution. Discussion of these issues has been made by Sandage & Tammann (1993) and need not be repeated here.

From the available data for 34 prototypical SNe Ia (i.e., those that do not show the types of peculiarities discussed above) in host galaxies with recession velocities $v_{220} > 1179$ km s^{-1} (and thus relatively free from noncosmological peculiar motion components), Sandage & Tammann (1993) have constructed Hubble diagrams relating peak observed magnitudes m_{pg}, m_B and m_V to the logarithm of the recession velocity. As discussed in detail in their § 2.1, the data fall along the required slope of $d \log v/d \log m = 0.2$ and show no systematic departure with apparent magnitude, as would be expected in a flux-limited sample if the distance indicator had significant intrinsic dispersion (the Malmquist bias). Rather, the data imply that the intrinsic standard deviation in peak magnitudes is smaller than 0.2 mag. The *random* scatter in the data are typically larger, ranging from 0.65 mag in $m_{pg}(\max)$ to 0.36 mag in $m_V(\max)$, and can be attributed to observational errors and some (but not very significant) extinction.

10.2. *The Value of H_0*

From the Hubble diagram in V (Sandage & Tammann 1993) for SNe Ia in host galaxies with velocities in the range $1179 \leq v_{220} \leq 15000$ km s^{-1}, we have

$$\log v = 0.2 m_V + 0.658 (\pm 0.012) , \quad (34)$$

and hence

$$\log H_0 = 0.2 M_V(\max) + 5.658 (\pm 0.012) , \quad (35)$$

where individual supernovae scatter in magnitude from the fitted regression with $\sigma_m = 0.36$ mag. The measured value of $M_V(\max)$ for SN 1937C then yields H_0. The uncertainty in the value derived in this way depends not only on the uncertainty in the determination of $M_V(\max)$, but also on the scatter in the observed m_V from individual SNe Ia in the Hubble diagram: taken in quadrature, this gives a net uncertainty $\delta M_V(\max) = 0.38$.

Differentiating equation (35), we can write

$$\frac{\delta H_0}{H_0} = 0.46 \delta M_V(\max) . \quad (36)$$

From equations (33), (35), and (36) we therefore obtain

$$H_0 = 52 \pm 9 \text{ km s}^{-1} \text{ Mpc}^{-1} . \quad (37)$$

Since the uncertainty is dominated by random scatter in the Hubble diagram, determination of $M_V(\max)$ for N calibrator SN Ia will reduce the uncertainty as $N^{0.5}$.

Future progress on H_0 has therefore to follow two routes:

1. Additional SNe Ia in or beyond the Virgo cluster and with accurate photometry near maximum will improve the definition of the Hubble line of equation (34).

2. New Cepheid distances to galaxies which have produced well-observed SNe Ia will clarify the role of SNe Ia as standard candles and reduce the random error of H_0. Corresponding steps are presently in progress.

L. L., H. S., and G. A. T. thank the Swiss National Science Foundation for financial support. We also thank Jerry Kristian and George Carlson for observing IC 4182 from Palomar to provide a ground-based check on the photometric cali-

bration. Thanks are due to all the behind-the-scene workers at the STScI whose efforts made the observations successful. A. S. (STScI) thanks John Krist for software efforts that have streamlined the variable search procedures. We again thank Paul Schechter for help with DoPHOT, which he developed under NSF grant AST83-18504.

REFERENCES

Arp, H. C. 1961, ApJ, 133, 871
Baade, W. 1944, ApJ, 100, 147
Baade, W., & Zwicky, F. 1938, ApJ, 88, 411
Barbon, R., Capaccioli, M., & Ciatti, F. 1975, A&A, 44, 267
Beyer, M. 1939, Astron. Nach., 268, 341
Branch, D. 1982, ApJ, 258, 35
Branch, D., & Bettis, C. 1978, AJ, 83, 224
Branch, D., & Tammann, G. A. 1992, ARA&A, 30, 359
Buonanno, R., Buscema, G., Corsi, C. E., Ferraro, I., & Iannicola, G. 1983, A&A, 126, 278
Buonanno, R., Corsi, C. E., De Biase, G. A., & Ferraro, I. 1979, in Image Processing in Astronomy, ed. G. Sedmak, M. Capaccioli, & R. J. Allen (Trieste: Osservatorio Astron. di Trieste), 354
Cadonau, R. 1987, Ph.D. thesis, Univ. of Basel
Cadonau, R., Sandage, A., & Tammann, G. A. 1985, in Lecture Notes in Physics, Vol. 224, Supernovae as Distance Indicators, ed. N. Bartel (Berlin: Springer-Verlag), 151
Della Valle, M., & Panagia, N. 1992, AJ, 104, 696
Feast, M., & Walker, A. R. 1987, ARA&A, 25, 345
Freedman, W. L., & Madore, B. F. 1990, ApJ, 365, 186
Harris, H. C., Baum, W. A., Hunter, D. A., & Kreidl, T. J. 1991, AJ, 101, 677
Hunter, D. A., Faber, S. M., Light, R., & Shaya, E. 1992, in Wide Field/Planetary Camera Final Orbital/Science Verification Report, ed. S. M. Faber (Baltimore: STScI)
Kowal, C. 1968, AJ, 73, 1021
Labhardt, L., & Sandage, A. 1993, in preparation
Labhardt, L., Schwengeler, H., & Tammann, G. A. 1993, ST-ECF Newsletter, 19, 13
Labhardt, L., Spaenhauer, A., & Schwengeler, H. 1991, in 3d ESO/ST-ECF Data Analysis Workshop, ed. P. J. Grosbøl & R. H. Warmels (Garching: ESO), 79
———. 1992, A&A, 265, 869
Lafler, J., & Kinman, T. D. 1965, ApJS, 11, 216
Landolt, A. U. 1973, AJ, 78, 959
Landolt, A. U. 1983, AJ, 88, 439
———. 1992, AJ, 104, 340
Lauer, T. E. 1992, in Wide Field/Planetary Camera Final Orbital/Science Verification Report, ed. S. M. Faber (Baltimore: STScI)
Leibundgut, B., Tammann, G. A., Cadonau, R., & Cerrito, D. 1991, A&AS, 89, 537
MacKenty, J. W., Schneider, G., Baggett, S. M., Mitchell, D. D., Ritchie, C. E., & Sparks, W. B. 1993, in SPIE Conf., Vol. 1945, ed. P. Bely & J. Breckenridge (Bellingham: SPIE), 340
Madore, B. F., & Freedman, W. L. 1991, PASP, 103, 933
Mateo, M., & Schechter, P. L. 1989, in Proc. 1st ESO/ST-ECF Workshop on Data Analysis, ed. P. J. Grosbol, F. Murtaugh, & R. H. Warmels (Garching: ESO)
Mihalas, D. 1963, PASP, 75, 256
Miller, D. L., & Branch, D. 1990, AJ, 100, 530
Moffat, A. F. J. 1969, A&A, 3, 455
Ratnatunga, K., & Bahcall, J. N. 1985, ApJS, 59, 63
Saha, A., & Hoessel, J. G. 1990, AJ, 99, 97
Sandage, A. 1957, ApJ, 125, 435
———. 1972, QJRAS, 13, 202
Sandage, A., & Tammann, G. A. 1968, ApJ, 151, 531
———. 1982, ApJ, 256, 339
———. 1993, ApJ, 415, 1
Sandage, A., Saha, A., Tammann, G. A., Panagia, N., & Macchetto, F. D. 1992, ApJ, 401, L7
Schechter, P. L., Mateo, M., & Saha, A. 1993, PASP, 105, 1342
Scheffler, H. 1982, in Landolt-Börnstein, Astronomy & Astrophysics, Vol. 2c, ed. K. Schaifers & H. H. Voight (Berlin: Springer-Verlag), 46
Stetson, P. B. 1987, PASP, 99, 191
Tammann, G. A. 1982, in Supernovae: A Survey of Current Research, ed. M. J. Rees & R. J. Stoneham (Dordrecht: Reidel), 371
Tammann, G. A., & Leibundgut, B. 1990, A&A, 236, 9
Westerlund, B. E. 1963, MNRAS, 127, 83